

AD-A136 313

LARGE-SCALE NUMERICAL ANALYSIS OF SEISMIC WAVES IN
BASINS(U) WEIDLINGER ASSOCIATES MENLO PARK CA

1/4

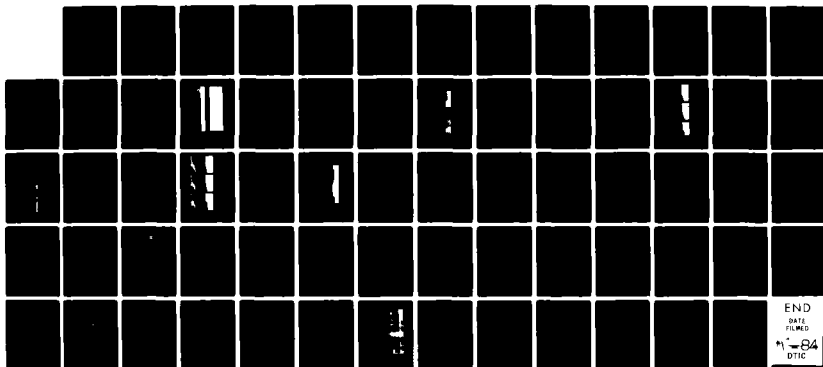
G L WOJCIK ET AL. 30 SEP 82 R-8241 AFOSR-TR-83-1229

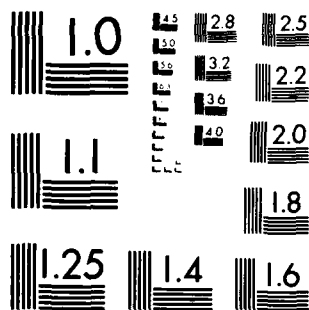
UNCLASSIFIED

F49620-82-C-0002

F/G 8/11

NL





MICROCOPY RESOLUTION TEST CHART
NATIONAL BUREAU OF STANDARDS 1963-A

12

R 8241 ✓

WEIDLINGER ASSOCIATES
3000 Sand Hill Road
Building 4, Suite 155
Menlo Park, California 94025

A136313

**LARGE-SCALE NUMERICAL ANALYSIS
OF SEISMIC WAVES IN BASINS**

By

G.L. Wojcik
J. Isenberg
D.K. Vaughan
R.E. Wolf

Prepared for

Air Force Office of Scientific Research
Bolling AFB, Washington, D.C. 20332

and

Air Force Geophysics Laboratory
Terrestrial Sciences Division
Hanscom AFB, Massachusetts 01731

DEC 27 1983
A

Interim Report

AFOSR Contract F49620-82-C-0002

For the Period 1 October 1981 to 30 September 1982

83 12 27

Copyright unlimited.

DTIC FILE COPY

UNCLASSIFIED

SECURITY CLASSIFICATION OF THIS PAGE (When Data Entered)

REPORT DOCUMENTATION PAGE		READ INSTRUCTIONS BEFORE COMPLETING FORM
1. REPORT NUMBER	2. GOVT ACCESSION NO.	3. RECIPIENT'S CATALOG NUMBER
AFOSR TR. 82-1229		
4. TITLE (and Subtitle) Large-Scale Numerical Analysis of Seismic Waves in Basins		5. TYPE OF REPORT & PERIOD COVERED Interim Report 1 Oct 1981 to 30 Sept 1982
		6. PERFORMING ORG. REPORT NUMBER R 8241
7. AUTHOR(s) G. L. Wojcik D. K. Vaughan J. Isenberg R. E. Wolf		8. CONTRACT OR GRANT NUMBER(s) F49620-82-C-0002
9. PERFORMING ORGANIZATION NAME AND ADDRESS Weidlinger Associates 3000 Sand Hill Road, 4-155 Menlo Park, CA 94025		10. PROGRAM ELEMENT, PROJECT, TASK AREA & WORK UNIT NUMBERS 61102F 2309/A1
11. CONTROLLING OFFICE NAME AND ADDRESS Air Force Office of Scientific Research/NP Building 410 Bolling AFB, Washington, D. C. 20332		12. REPORT DATE 30 Sept 82
		13. NUMBER OF PAGES 65
14. MONITORING AGENCY NAME & ADDRESS (if different from Controlling Office)		15. SECURITY CLASS. (of this report) UNCLASSIFIED
		15a. DECLASSIFICATION/DOWNGRADING SCHEDULE
16. DISTRIBUTION STATEMENT (of this Report) Approved for public release; distribution unlimited.		
17. DISTRIBUTION STATEMENT (for the abstract entered in Block 20, if different from Report)		
18. SUPPLEMENTARY NOTES		
19. KEY WORDS (Continue on reverse side if necessary and identify by block number) Basin and Range geology large-scale finite element analysis full-field synthetic seismograms		
20. ABSTRACT (Continue on reverse side if necessary and identify by block number) -This report describes the application of a large-scale numerical wave solver to the time domain study of seismic wave phenomena in basins typical of the Basin and Range province. The solver uses an explicit finite element algorithm designed for fully vectorized execution on the CRAY-1. Calculations were performed to study the effects of basin edge geometry on reflection and transmission of body and surface waves. Normal and tangential surface traction sources were applied on the model centerline. From the resulting full wave field solution, synthetic seismograms were generated and used to quantify principal phases. In addition,		

DD FORM 1 JAN 73 1473

EDITION OF 1 NOV 55 IS OBSOLETE

UNCLASSIFIED

SECURITY CLASSIFICATION OF THIS PAGE (When Data Entered)

UNCLASSIFIED

20. ABSTRACT (concluded)

- the body and surface wave interaction of two basins separated by a mountain was studied. This model required 120,000 elements and demonstrated that large-scale full wave field calculations are practical on the CRAY-1.

The suite of calculations showed a number of differences between a steep faulted flank, an echelon faulted flank and a dipping flank. Basin edges are efficient transmitters of Rayleigh waves, apparently independent of edge details; however, geometry has a strong effect on Rayleigh wave reflection. Shear waves outside the basin depend markedly on edge geometry due to mode conversion of waves in the interior. Also, details of mode conversion at the basin edge depend on source type. The strong shear phase generated by the tangential source is converted primarily to S-waves at the edge, whereas the shear phase from the normal source is converted primarily to Rayleigh waves. The basin-range-basin model extends these results and provides insight into the type and strength of signals communicated between basins. It may indicate the extent to which seismic sources within a basin might be concealed from detection in an adjacent basin.

Theoretical finite element work showed that, in the context of cartesian finite element grids, the governing equations can be greatly simplified to reduce the arithmetic operations count and also formulated to admit selective damping on pure shear and dilatational modes of deformation.

UNCLASSIFIED

ACKNOWLEDGMENTS

The technical assistance of Myrtle Carey, Penny Sevison and Edith Durfey in report preparation is gratefully acknowledged.



DTIC	
COPY	
INSPECTED	
1	
Distribution	
Availability	
Accession	
List	
H-1	

U.S. DEPARTMENT OF SCIENTIFIC RESEARCH
TECHNICAL INFORMATION DIVISION

Chief, Technical Information Division

CONTENTS

<u>Section</u>	<u>Page</u>
1 INTRODUCTION	1
2 FULL FIELD SEISMIC RESPONSE IN BASINS	2
2.1 Geologic Models	2
2.2 Velocity Models	4
2.3 Finite Element Models	8
2.4 Synthetic Seismograms	10
2.5 The Layer/Halfspace With Constant Velocity	12
2.6 The Layer/Halfspace With Linear Velocity	14
2.7 Basins With Constant Velocity	16
2.8 Basins With Linear Velocity	19
2.9 Basins With Tangential Surface Traction	22
2.10 The Basin-Range-Basin Model	24
2.11 Selected Particle Motion Plots	28
3 THE FULL WAVE FIELD SOLVER	32
3.1 Background	32
3.2 Computational Mesh	34
3.3 The Finite Element Approximation	37
3.4 The Canonical Finite Element Basis	41
3.5 Canonical Element Dynamics	45
3.6 Explicit Integration and the Lumped Mass Approximation	48
3.7 Further Development	51
4 SUMMARY AND CONCLUSIONS	53
4.1 Summary of Calculations	53
4.2 Summary of Finite Element Theory	56
4.3 Conclusions	58
REFERENCES	60

ILLUSTRATIONS

<u>Figure</u>		<u>Page</u>
2-1	A schematic of the graben structure caused by deep seated extension and block subsidence in the Basin and Range province	3
2-2	Nominal Basin and Range graben basin, 16 km wide and 2 km deep with faulted flanks dipping at approximately 60 degrees	3
2-3	Layer and basin cross sections for numerical analysis of edge effects. Basins are 2 km deep and 8 km from centerline to edge	5
2-4	Two-basin model with an intervening mountain range, 16 km wide and 1 km high	5
2-5	Velocity functions assumed for basin fills and surrounding bedrock. Basin data compiled by Battis (1981) and crustal gradients derived from Prodehl (1979)	6
2-6	Finite element model layout of 7 x 20 km basin model (top); blowup of discrete elements (3 x 10 km) around the stepped flank basin edge (bottom)	9
2-7	Vertical velocity seismograms for the layered models with normal surface traction at the centerline convolved with 2 Hz wavelet. Lower suite is normalized by Rayleigh amplitude at 300 m and upper suite is magnified by 10 and truncated	13
2-8	Vertical velocity seismograms for the constant velocity basin models with normal surface traction	17
2-9	Ray diagrams for the piecewise constant velocity function illustrating the corner diffracted arrivals excited by head waves on the interface (critical angle = 34°)	18
2-10	Vertical velocity seismograms for the piecewise linear velocity models with normal surface traction	20
2-11	Vertical velocity seismograms for the piecewise linear velocity models with tangential surface traction	23
2-12	Vertical velocity seismograms for the basin-range-basin model with piecewise linear velocity and normal surface traction	25
2-13	Particle motion plots for the three basin types with velocity gradients and normal surface traction	29

ILLUSTRATIONS (Concluded)

<u>Figure</u>		<u>Page</u>
2-14	Particle motion plots for tangential surface traction on the echelon faulted flank	30
2-15	Particle motion plots for the basin-range-basin model with normal surface traction	30
3-1	Example of a cartesian mesh with equidistant grid lines, and the stepwise resolution of geology (c.f. Fig. 2-1)	36
3-2	Cartesian grid and element coordinate system	36
3-3	The normalized orthogonal cartesian displacement modes of a 2-D continuum element	43
3-4	Free vibration modes and frequencies in the canonical finite element basis. The reduced frequency is $\Omega \equiv \sqrt{2/3}\omega\Delta x/c_s$ and the signs at node 1 correspond to those of the x component mode assumed in Fig. 3-3. The wavespeed ratio, c_p/c_s , is denoted by k	47
3-5	A schematic of dynamic interaction between nodes for various Δt measured by the central node's circle of influence (sonic circle)	49
4-1	A schematic of travel time curves for the principal phases observed in basin flank synthetic seismograms	59

SECTION 1

INTRODUCTION

This report describes the application of a large-scale numerical wave solver to the time domain study of seismic wave phenomena in filled basins. The solver uses an explicit finite element algorithm designed for fully vectorized execution on the CRAY-1, permitting the solution of discrete hyperbolic problems on a scale at least one order of magnitude faster than conventional scalar machines allow (e.g., CDC 7600). This computing power is sufficient to analyze large 2-D inhomogeneous sections of the Earth's upper crust with, for example, a minimum of 2 Hz frequency resolution of Rayleigh and shear waves in a 50 km x 7 km grid (120 x 1000 elements). Such geologic models are essential to the present study of body and surface wave propagation in realistic basin structure, particularly the questions of edge effects, Rayleigh wave interactions, and wave coupling between basins on either side of a mountain. Because large scale computing is fairly new, the numerical modeling aspects of the problem are described in detail with emphasis on wave solver mechanics.

In Section 2, a set of four basin configurations are analyzed for two loading conditions and two velocity functions. The three single basin models include a steep faulted flank, an echelon faulted flank and a dipping flank. A larger scale basin-range-basin model completes the set. Full-field synthetic seismograms are displayed and interpreted for each model. In Section 3, the finite element theory is described for a cartesian computational mesh. The emphasis is on methods of reducing the operations count to minimize computer processing time. In Section 4, the calculations and theory are summarized and conclusions drawn.

SECTION 2

FULL-FIELD SEISMIC RESPONSE IN BASINS

The two-dimensional numerical calculations described in this section include a layered halfspace model and three symmetric basin models indicative of local geologies in the Basin and Range province of the western United States. In addition a larger model of two basins separated by a mountain range is used to investigate the degree of seismic coupling between basins. Near-surface seismic velocity functions are constructed using typical data compiled by Battis (1981) from a variety of Basin and Range studies. Velocity gradients in bedrock are taken from Prodehl (1979), based on USGS crustal refraction data. Vertical and horizontal surface loadings on the model centerline provide the seismic input, while vertical velocity seismograms and particle motion plots are used to interpret response.

2.1 Geologic Models

The Basin and Range province is characterized by east-west lateral extension, crustal thinning and uplift forming many parallel faults trending north-south. The resulting topography consists of parallel, elongated basins separated by narrow mountain ranges. The formative mechanism is thought to be block subsidence due to extension, Stewart (1971), although secondary block tilting may also be significant. A schematic illustration is given in Fig. 2-1. The resulting horst and graben model involves high angle faulting with typical dips between 45 and 70 degrees and fault throws on the order of a kilometer or more. Average basin depth is 2 km, width is 15 to 20 km, and length is approximately 70 km. The intervening mountain ranges are usually about 15 km wide and maximum elevation above basin fill may range from 0.3 to 1.2 km. These typical data were compiled by Battis (1981) in a study of the open literature on Basin and Range geology and tectonics.

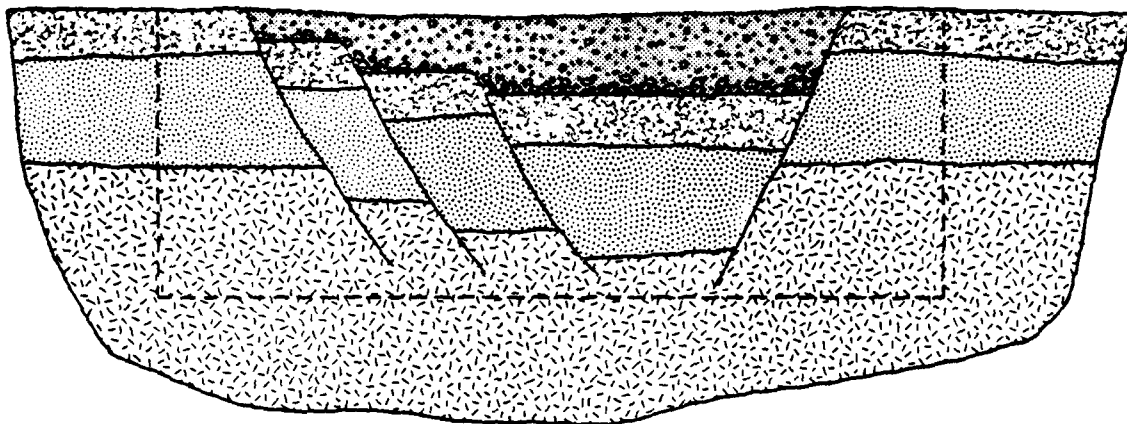


Figure 2-1. A schematic of the graben structure caused by deep seated extension and block subsidence in the Basin and Range province.

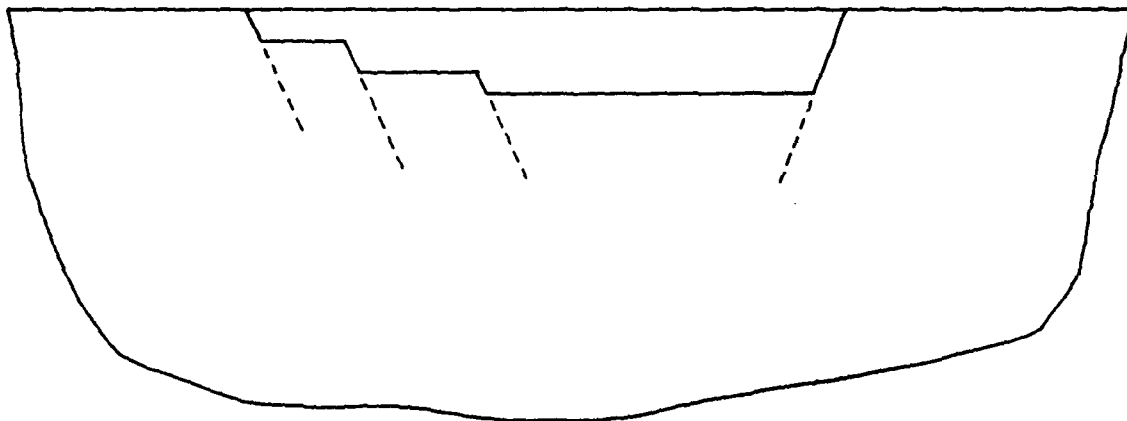


Figure 2-2. Nominal Basin and Range graben basin, 16 km wide and 2 km deep with faulted flanks dipping at approximately 60 degrees.

Based on the above data, a nominal basin is assumed to be 2 km deep and 16 km wide, with normal faulted flanks dipping at approximately 60 degrees. The length is assumed to be four times the width--sufficient to justify a two-dimensional model of the structure for numerical analysis. Such a basin is illustrated in Fig. 2-2 for the asymmetric faulting case. This cross section suggests the models for numerical study shown in Fig. 2-3. The simple layer model, Fig. 2-3a, establishes a baseline for response in the basin fill, without edge effects. The basin models, Fig. 2-3b,c,d, provide three types of edges--a single faulted flank (b), an echelon faulted flank (c), and a shallow dipping flank (d) which is the limiting case of echelon faults. These models assume symmetry across the basin axis in order to minimize problems. Some effects of asymmetry can be estimated from them. On a larger scale, Fig. 2-4 shows the two-basin model with an intervening mountain range. Height and width of the range are taken as 1 km and 16 km, respectively.

2.2 Velocity Models

The graben basins have been continually filled during their development--predominantly with alluvium from stream erosion of neighboring mountains, but with significant ash and lava deposits during periods of volcanism. The surrounding crustal blocks include a variety of sedimentary, volcanic, and plutonic rock types. This situation indicates a highly inhomogeneous velocity distribution for the basin fill and bedrock.

Basin seismic velocities are tabulated by Battis (1981) from studies by Thompson, et al. (1967) and Healy and Press (1964). The average P-wave velocities and bounds are shown in Fig. 2-5a. Superposed on these is a linear approximation to the average, starting at 2 km/sec on the free surface with

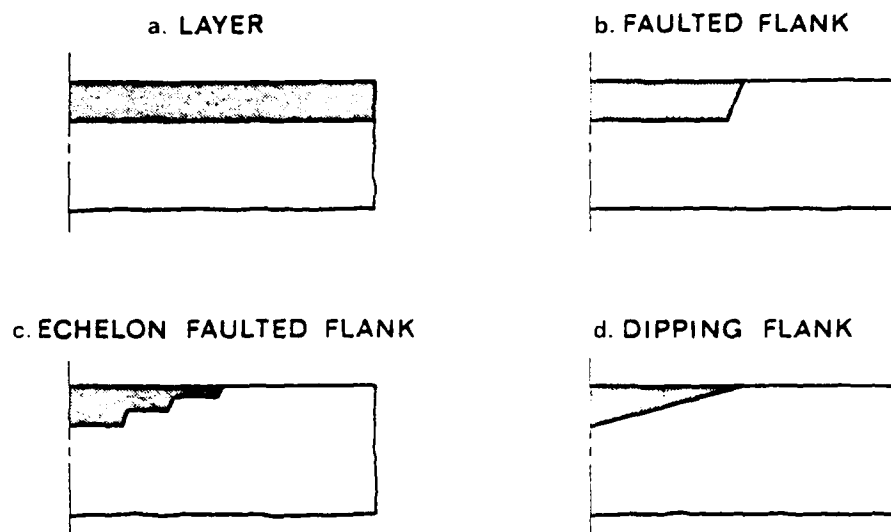


Figure 2-3. Layer and basin cross sections for numerical analysis of edge effects. Basins are 2 km deep and 8 km from centerline to edge.

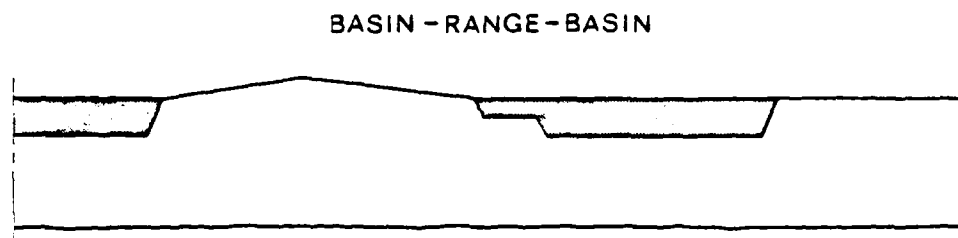
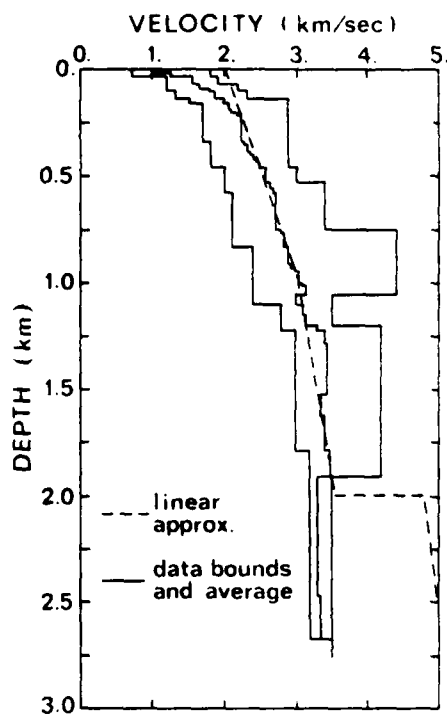
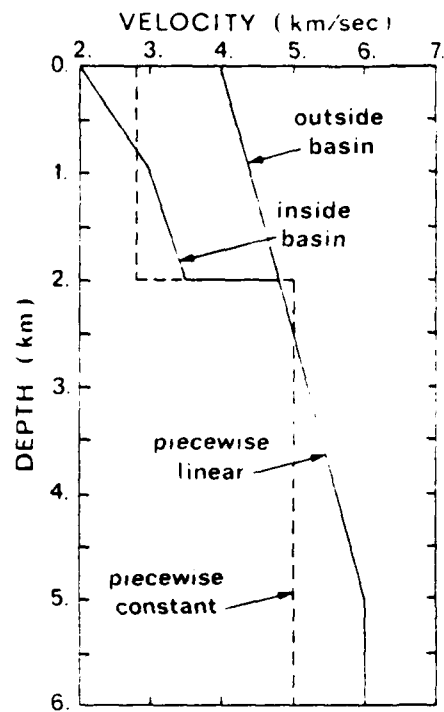


Figure 2-4. Two-basin model with an intervening mountain range, 16 km wide and 1 km high.



a. BASIN VELOCITY MODEL



b. UPPER CRUST VELOCITY MODEL

Figure 2-5. Velocity functions assumed for basin fills and surrounding bedrock. Basin data compiled by Battis (1981) and crustal gradients derived from Prodehl (1979).

a 1 km/sec/km gradient down to 1 km depth and a 0.5 km/sec/km gradient to 2 km where the velocity is 3.5 km/sec. This approximation ignores the low speed surface layer with velocity between 1 and 2 km/sec in the upper 0.2 km. Of course, the average data does not indicate lateral variations in velocity across the basin due to differences between interior (flats or playa) and perimeter (alluvial fan) deposits; nor does it include volcanic anomalies like intrusions, old surface flows, etc. These will be neglected here in comparison to the lateral change between alluvium and bedrock properties at the basin edge.

Bedrock seismic velocities have not been studied to the extent that basin velocities have; however, estimates from in-situ measurements of exposed bedrock indicate a range from 4.7 to 5.1 km/sec, Thompson et al. (1967). The variation of bedrock velocity with depth is not known. USGS crustal refraction data in the Basin and Range, reduced by Prodehl (1979) yield a crude estimate of the upper crust gradient at 0.4 km/sec.km. This is based on a surface velocity of 4 km/sec varying smoothly to 6 km/sec at 5 km depth, from Prodehl's velocity function drawings. The actual gradient is probably not constant and could easily be half the above value, assuming a surface velocity of 5 km/sec for example. The resulting upper crust velocity model is shown in Fig. 2-5b. At 2 km depth the P-wave velocity is 4.8 km/sec rising linearly to 6 km/sec at 5 km depth. Below 5 km the data show a very low gradient, hence a constant velocity is assumed. A piecewise constant model is also drawn in the figure, with 2.8 km/sec in the basin fill and 5 km/sec in the rock. This choice of basin velocity gives the same vertical transit time as the piecewise linear model.

The remaining seismic data needed for analysis are S-wave velocities and material densities. A good S-wave approximation for the deeper basin

fill and bedrock is the Poisson assumption, $\nu = 0.25$ giving a ratio of P to S velocity of $V_p/V_s = \sqrt{3}$. For simplicity, this will also be used for the shallow basin fill, although data show that the ratio is generally higher for the weathered layer. Densities are assumed to be 2.2 gm/cm^3 for alluvium and 2.5 gm/cm^3 for bedrock. These values are probably within 10 to 15 percent of the actual depth dependent densities.

2.3 Finite Element Models

The geologic cross sections in Figs. 2-3,4 are modeled by cartesian, plane strain finite element grids. A $7 \times 20 \text{ km}$ model for the echelon faulted flank case, Fig. 2-3c, is illustrated in Fig. 2-6, for example. Boundary conditions are such that the surface is traction free, the left side is a line of symmetry, while the right and bottom sides are transmitting boundaries (normal impedance type). Only seismic line sources on the surface are considered, consisting of normal or tangential tractions in a Gaussian distribution over a few nodes about the model centerline. This spread of surface loading is necessary to minimize nonphysical element deformational modes associated with single node forcing functions.

Element size depends on the minimum wavelength to be resolved. From the velocity functions described above, clearly the slowest phase in these models will be the Rayleigh surface wave, for which $V_R \approx 0.919 V_S \geq 1.06 \text{ km/sec}$ (based on $V_S = V_p/\sqrt{3} \approx 1616 \text{ km/sec}$ at the free surface). Assuming the maximum frequency of interest is 2 Hz (1/2 second period) then the minimum wavelength is 503 meters. The minimum number of elements per wavelength is no less than 10, whence the maximum element size is 50 meters. To gage whether 10 elements per wavelength is adequate, it is sufficient to compare maximum input frequency to the minimum natural frequency of 50 meter square elements. From

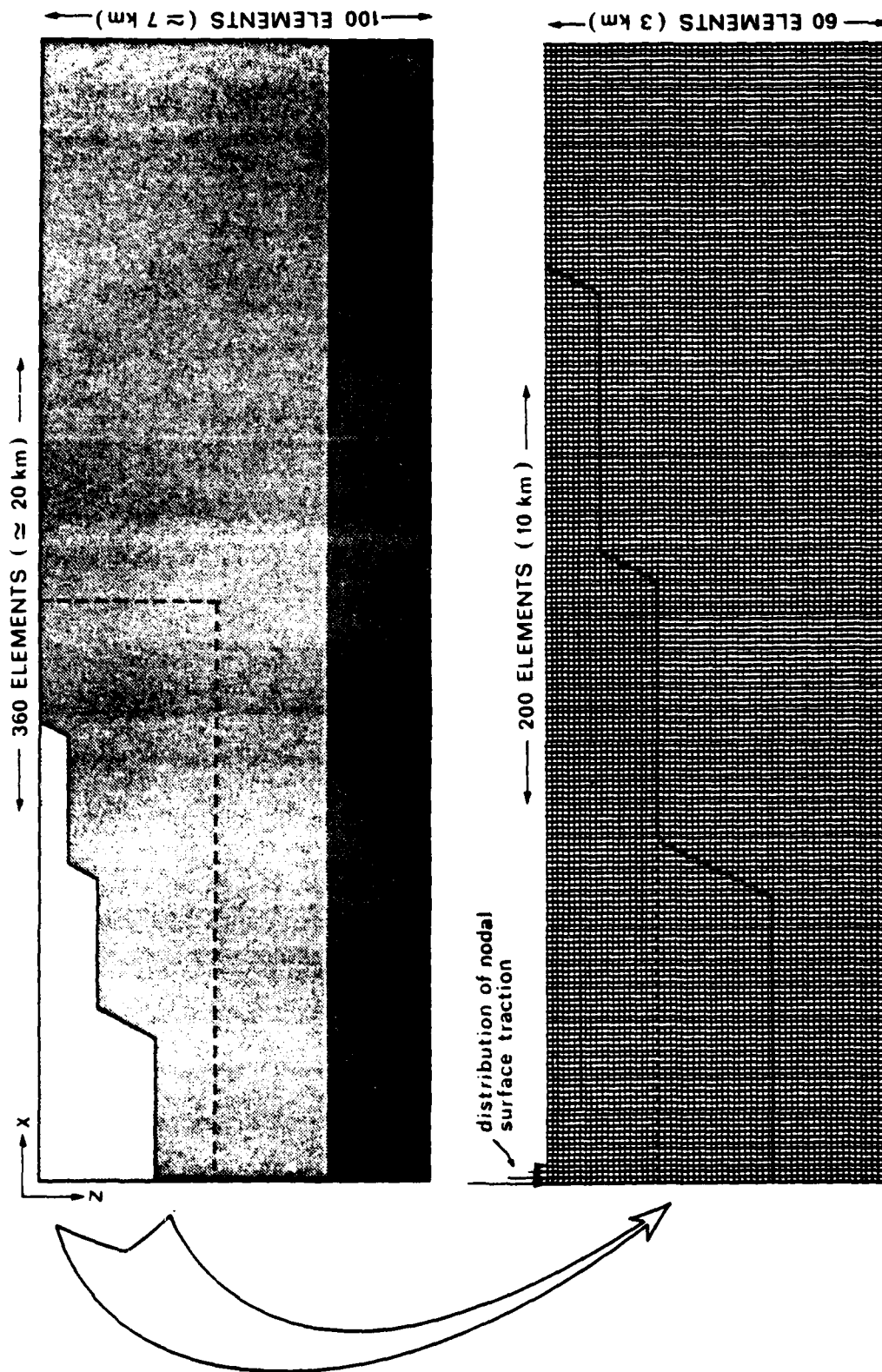


Figure 2-6. Finite element model layout of 7 x 20 km basin model (top); blowup of discrete elements (3 x 10 km) around the stepped flank basin edge (bottom).

Section 3.5, $f_N = 1/T_N \approx V_P/(8.89\Delta x) \approx 4.45$ Hz, hence the input of 2 Hz is less than half the element ringing frequency and adequate for modeling purposes.

Because the normal impedance type transmitting boundary conditions used here are not perfect, some energy will be reflected back into the grid. To minimize the possibility of confusing reflected phases from the boundary with refracted phases, elements are graded in size near the boundary to introduce dispersion and scattering. Therefore, elements are made square in a 3 x 16 km strip including the basin in Fig. 2-6, but are graded by 3 percent per element to the bottom and right boundaries yielding a maximum element aspect ratio of 3 there. This is a crude solution at best to the transmitting boundary problem and will be evaluated later.

The resulting finite element models to be solved on the CRAY-1 contain 36,000 elements for each of the basin flank cases shown in Fig. 2-3, and 120,000 elements for the basin-range-basin model in Fig. 2-4. The explicit finite element code used (for which the theory is described in Section 3) requires two microseconds (2×10^{-6} sec) to evolve each element one timestep. The timestep is taken as 80 percent of the minimum element transit time which, from Fig. 2-5, gives 6.7 milliseconds (6.7×10^{-3} sec) for 50 m elements. Finite element run times are chosen to propagate the free surface Rayleigh wave across the model (approximately) requiring 1500 timesteps for the constant velocity flanks, 2000 steps for the variable velocity flanks and 5000 steps for the basin-range-basin case. Multiplying number of model elements by number of timesteps gives 54×10^6 , 72×10^6 and 6×10^8 element-timesteps, respectively, for these cases, requiring 108, 145 and 1200 seconds for their execution.

2.4 Synthetic Seismograms

Model response to the surface traction inputs is recorded at many output points over the free surface, and also through depth at selected ranges.

Only surface response is examined here, however. Because the model is linear (small displacements), it suffices to use a Green's function formulation, i.e., the original source time function is a generalized function (delta function, step, etc.). Any desired time history may then be obtained by convolution (Duhamel superposition). Of course, frequency resolution is no better than the original finite element grid will allow. Thus, from a single finite element run, synthetics are constructed for any source time function. The effect of instrument response, if necessary, is included by a second convolution. A change in source type or addition of new structure to the model requires a new finite element run.

Before examining model response, some comments on interpretation are in order. The suite of synthetics typically shows a number of phases identified by their correlation in space and time from one trace to the next. There are a variety of tools available to aid in extracting quantitative information from the synthetics. One is a correlation function to track phases (stationary phase points) automatically yielding travel time curves, phase velocities, etc; and another is beam-forming to determine the direction of incident waves. In the following, only qualitative results (visual correlations) are discussed but it will be clear that quantitative tools in conjunction with finite element solutions offer major advantages. Another comment concerns the effect of structural modifications in the model. These are easily found by subtracting the original and modified suite of synthetics, showing seismic influence independently of the complete seismogram (which contains a variety of strong phases masking subtle structural effects). Applications include effects of local changes in wavespeed due to inclusions and cavities, corner diffractors, etc. Finally, it should be recognized that detailed interpretation of seismograms requires a ray tracing capability in inhomogeneous media. Therefore, to

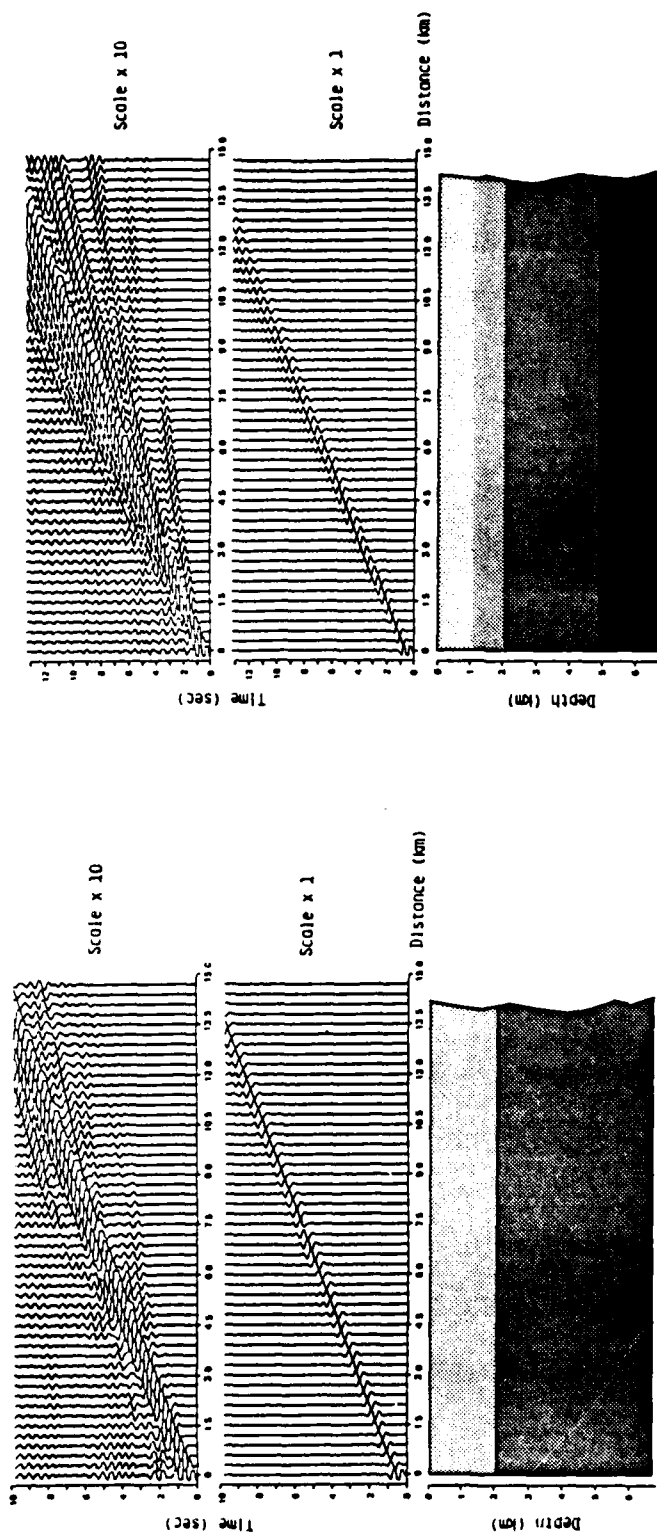
quantify aspects of the following visual interpretations, a two-point ray tracing analysis would be useful and some will be described in the final report.

2.5 The Layer/Halfspace With Constant Velocity

To establish a baseline for subsequent basin analyses, it is useful to start with the simple layer model loaded by normal surface traction at the origin. This first calculation assumes the piecewise constant velocity function in Fig. 2-5b. The model and vertical velocity seismograms are shown in Fig. 2-7a. The Green's function is convolved with a 2 Hz wavelet for these synthetics and amplitude is normalized by the Rayleigh wave maximum on the second trace, 300 meters from the origin. The dominant phase is clearly the Rayleigh wave and to see the body waves each trace is multiplied by 10 and truncated as shown in the upper suite. Data was collected at a finer spatial increment but the 300 meter spacing in the figure is convenient for visual interpretation.

Slope of the Rayleigh wave arrivals (time-distance curve) in Fig. 2-7a yields a phase velocity of approximately 1.45 km/sec, which is 2.4 percent lower than the theoretical value for a halfspace of the layer medium (basin fill) only. Because the wavelength is 0.743 km (providing 15 elements per wavelength) the 2 km interface is 2.69 wavelengths below the surface, hence the surface wave is barely affected by the faster halfspace. The 2.4 percent discrepancy between exact and measured phase velocity is caused by the discrete finite element model--a combination of discrete data (15 elements per wavelength), the lumped mass approximation, and reduced stiffness of element bending modes.

Body waves are much lower in amplitude and more complicated to interpret than surface waves. The body wave arrivals in Fig. 2-7a are a summation of direct waves in the layer, reflected waves from the interface and head waves.



a. Constant velocity layer model

b. Piecewise linear velocity layer model

Figure 2-7. Vertical velocity seismograms for the layered models with normal surface traction at the centerline convolved with 2 Hz wavelet. Lower suite is normalized by Rayleigh amplitude at 300 m and upper suite is magnified by 10 and truncated. Spacing between output points on the surface is 300 meters.

The direct P-wave grazing the surface is the first arrival out to a range of 3.35 km, after which head waves overtake it. The head wave begins at the critical range of 2.71 km (travel time = 1.67 sec) and is seen most distinctly as the very low amplitude first arrival beyond 9 km. Reflected waves from the interface follow the direct P-wave and are seen in the range from 0 to 1.5 km with peak amplitude arriving at about 2 sec (first arrival at 1.43 sec.). This arrival is obscured by the Rayleigh wave from 1.5 to 4 km and reappears at 4 km out to 8 km or so, but beyond amplitude drops considerably. The change in amplitude is caused by constructive interference of direct, reflected and head waves in the range from 4 to 8 km due to closely spaced arrival times. Beyond 8 km the arrivals are separated in time and do not interfere significantly.

The S-wave phases at any range follow the same travel path as corresponding P-waves (because V_p/V_s is constant over the model), but have travel time .3 longer. They are obscured by the Rayleigh wave out to 8 km and are difficult to pick thereafter, probably because of constructive interference by P-wave multiples. This interference begins to form a ducted Rayleigh wave beyond 9 km (starting at 6 sec.).

Reflections from the model boundary, although minimized, are still in evidence, particularly near the origin at 4 and 8 seconds. These dispersed wavetrains are principally reflected from the graded elements rather than the boundary itself, and their influence downrange is difficult to assess. However, based on the absence of clear reflected phases prior to the Rayleigh wave arrival, the boundary reflections downrange appear to be minimal. Behind the Rayleigh wave this may not be the case.

2.6 The Layer/Halfspace With Linear Velocity

The second layer calculation uses the same finite element model as above but with the piecewise linear velocity function in Fig. 2-5a; again loaded by

normal surface traction at the origin. Normalized seismograms for the 2 Hz wavelet are shown in Fig. 2-7b. The Rayleigh wave is clearly more dispersed in this case, caused in large part by the velocity gradient--but also increased by coarser frequency resolution near the free surface (10 elements/wavelength rather than 16 as in Fig. 2-7a). The dispersion is readily seen by viewing obliquely along the crest of the phase in Fig. 2-7b. At any range, phase velocity, measured by the local slope of a line connecting stationary phase points, is approximately constant; but time of peak amplitude arrival is continuously retarded.

Body waves are seen to be stronger phases in this case due to the linear gradient. The arrivals now consist of refracted waves in the layer, reflected waves from the interface discontinuity and refracted waves in the underlying bedrock. The piecewise linear velocity gradient curves the wavefronts and rays and reduces the head wave to insignificance in comparison to the analogous refracted wave. The predominant first arrivals in the range out to 4 km are refracted P-waves in the layer. Between 4 and 7.5 km the arrivals are strengthened by constructive interference of reflected and refracted bedrock waves in addition to refracted basin waves; and beyond 7.5 km the arrival is predominantly refracted through bedrock (corresponding to head waves in the constant velocity model).

Distinctive S-wave phases are more difficult to identify because of interference by other arrivals--Rayleigh waves close-in and constructively interfering P-wave multiples further out. Refracted basin S-waves are clearest at intermediate range, between 6 km and 7.5 km for example, with 4 to 5 second arrival time. Refracted bedrock S-wave arrivals continue smoothly from the basin phase beyond 7.5 km but are preceded by a P-wave phase (between 10.5 and 13.5 km) and followed by an S-wave phase (both identified

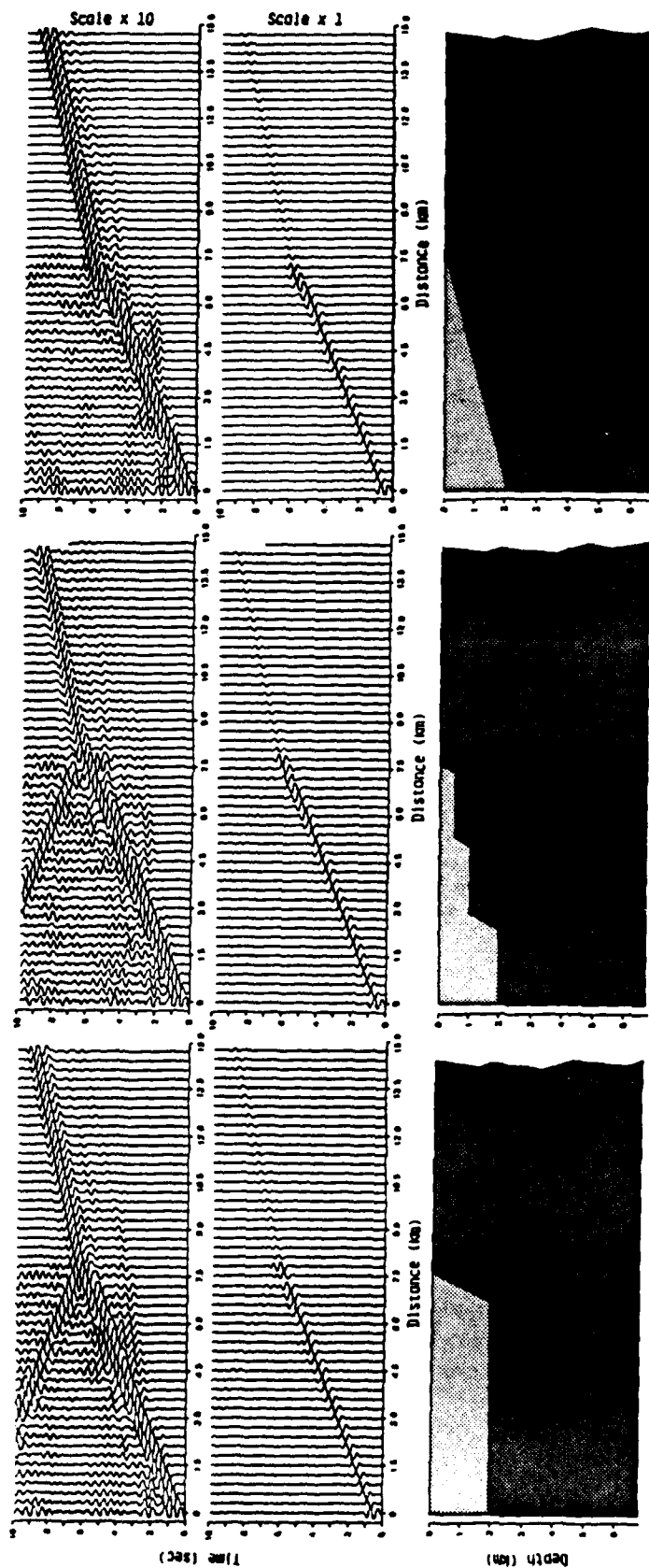
on the basis of travel-time slope, i.e., phase velocity). These are probably the result of multiple P- and S-wave refractions and mode conversion, although a detailed ray analysis would be necessary to confirm this.

Comparing seismograms in Fig. 2-7a and 2-7b close to the origin shows that reflections off the bottom model boundary are lower amplitude and less coherent for the linear velocity structure. This follows because the element grading effect is similar to that produced by the velocity gradient. In addition, the curving of rays (energy travel paths) in the model turn much of the downward propagating energy back towards the surface. Based on these observations the grading and transmitting boundary conditions appear to perform adequately for the linear velocity models.

2.7 Basins With Constant Velocity

Analysis of basin response will begin by considering the piecewise constant velocity function in the three basin models. The models and 2 Hz synthetics are displayed in Fig. 2-8a,b,c. Basin flanks are resolved in the stepwise fashion indicated in Fig. 2-6. In comparison to the layer results, the distinctive feature of these seismograms is transmission and reflection of the Rayleigh wave at the basin boundary 8 km from the center-line (line of symmetry). Comparing the magnified seismograms shows that the steep faulted flank (Fig. 2-8a) is the most effective reflector, the echelon faulted flank (Fig. 2-8b) is somewhat less effective, and the dipping flank (Fig. 2-8c) is a relatively poor reflector. However, in terms of transmission, the steep and dipping flanks are comparable, and both are better transmitters than the echelon flank.

The body wave phases over the basin are composed of direct and multiply reflected waves, head waves, and diffracted waves from the corners. At close



a. Steep faulted flank b. Echelon faulted flank c. Dipping flank

Figure 2-8. Vertical velocity seismograms for the constant velocity basin models with normal surface traction.

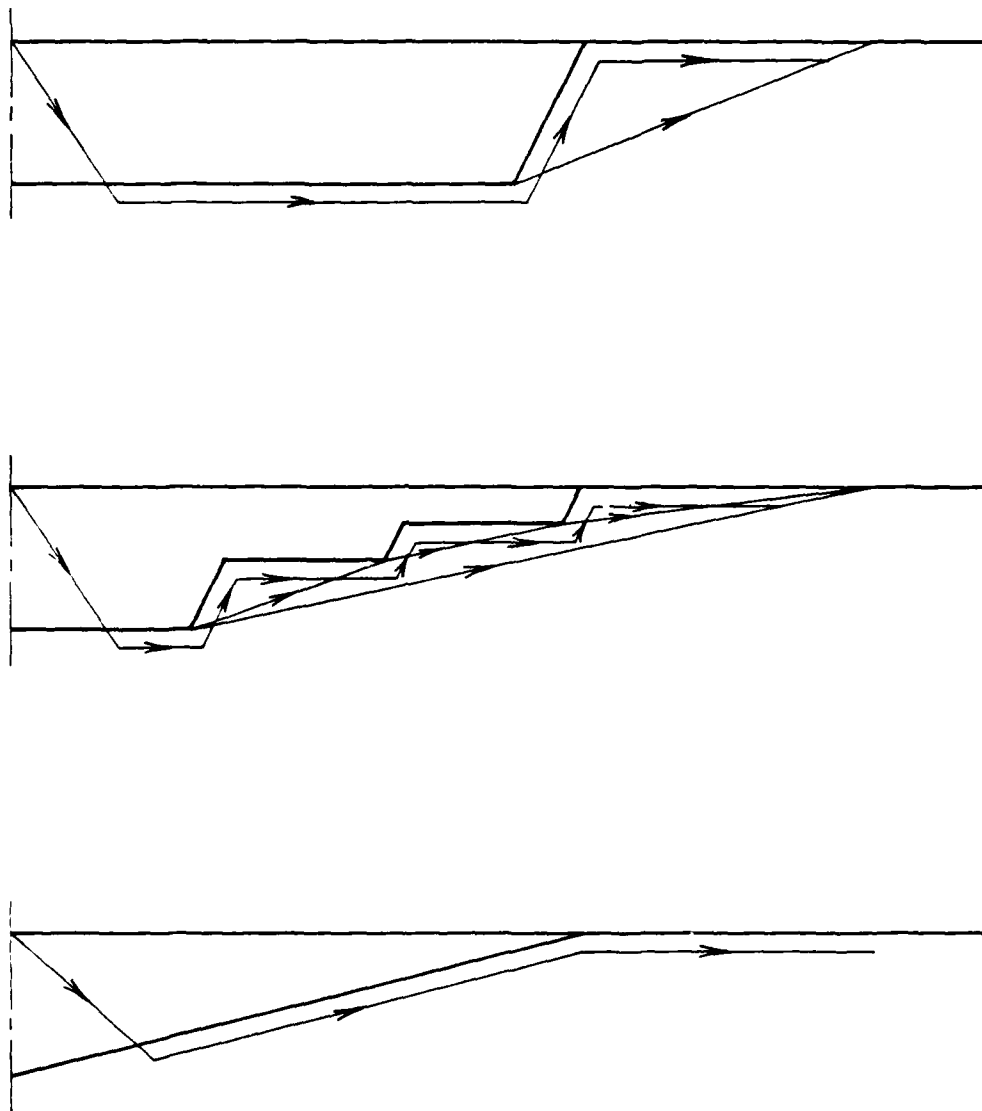


Figure 2-9. Ray diagrams for the piecewise constant velocity function illustrating the corner diffracted arrivals excited by head waves on the interface (critical angle = 34°).

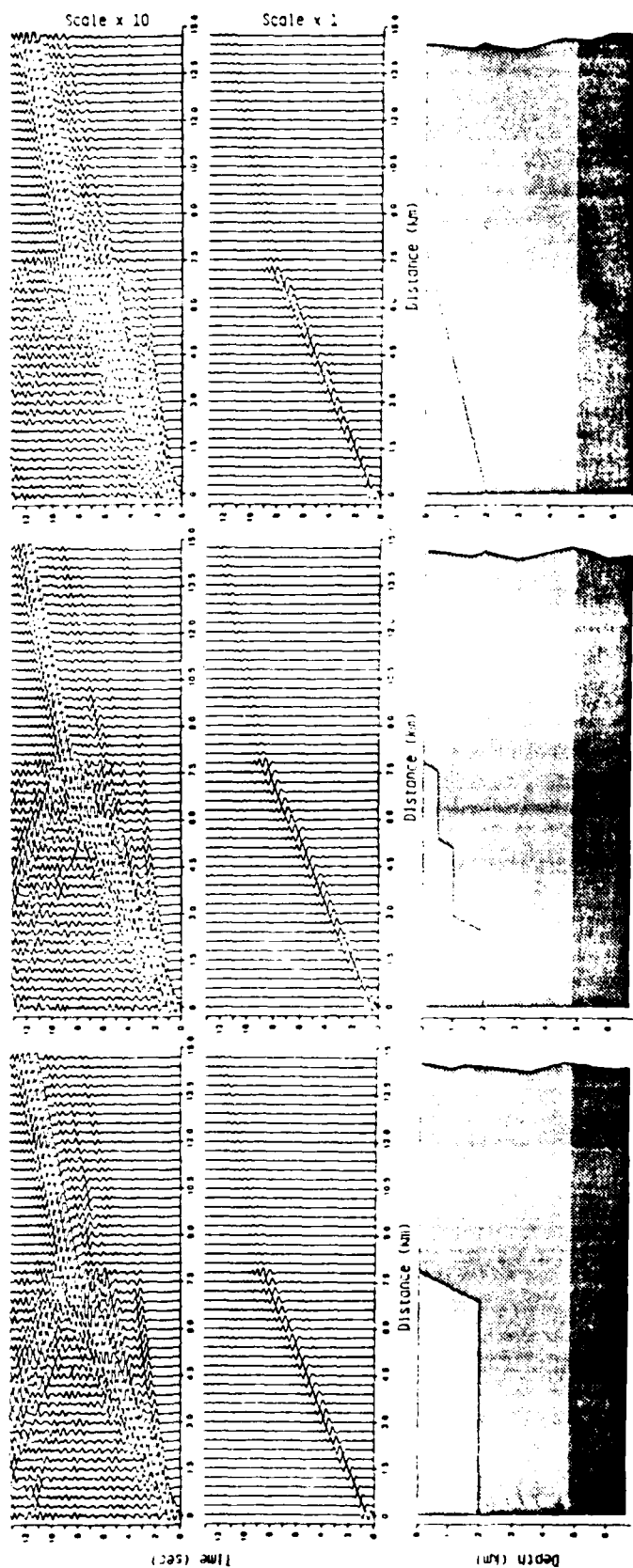
range (out to 3 or 4 km) the first arrivals are direct P-waves and are the same for each model. Later arrivals are masked by the Rayleigh wave. At intermediate range, to the basin edge, the arrivals are modified by the flank. For the steep flank the constructively interfering phases are virtually identical to the layer case in Fig. 2-7a. However, for the echelon and dipping flank, the intermediate range arrivals constructively interfere over a shorter segment on the surface but yield about the same amplitude.

Outside the basin the leading body wave arrivals are due entirely to diffractions from the corners on the interface. They are caused by the head wave traveling along the interface and exciting diffracted waves as each corner is encountered. Elementary ray diagrams illustrating the process are drawn in Fig. 2-9. Further magnification of the seismograms is necessary to clearly identify these phases, as they are weak in the bedrock.

The later phases outside the basin are due to direct body and surface waves within the basin interacting with the corners. The strongest is, of course, the transmitted surface wave, but it is preceded by a sequence of weaker Rayleigh waves excited by the mode conversion of direct body, head, and diffracted waves at the surface corner. These can be seen as leading phases parallel to the transmitted Rayleigh phase, and are easily identified by viewing obliquely from the origin along this strong phase. The most distinct example is for the steep flank in Fig. 2-8, where direct body waves are partially converted to surface waves at the corner starting at 3 to 3.5 sec. Note that this mode conversion also excites body waves outside which are too weak to see in the seismograms.

2.8 Basins With Linear Velocity

Synthetics for the three basin models with piecewise linear velocity functions and normal surface traction at the origin are pictured in Fig. 2-10.



a. Steep faulted flank

b. Echelon faulted flank

c. Dipping flank

Figure 2-10. Vertical velocity seismograms for the piecewise linear velocity models with normal surface traction.

In these cases, the seismograms indicate that steep and echelon faulted flanks (Fig. 2-10a,b) are the more effective reflectors of Rayleigh waves, while the dipping flank (Fig. 2-10c) is a poor reflector. In terms of Rayleigh wave transmission, the three basin flanks appear to be comparable. These conclusions are consistent with the previous case of constant velocity basins.

The body wave phases within the basins are similar to those described for the layer with linear velocity. The first arrivals out to about 4.5 km are reflected P-waves in the basin. From 4.5 km to the basin edge, the arrivals also include reflected and refracted bedrock waves, as well as diffracted waves from the interface edges. However, the arrival sequence is difficult to interpret from these relatively low frequency seismograms. Better resolution would require higher frequencies, hence finer grid spacing in and around the basin. In both the echelon faulted and dipping flank cases, the body wave amplitude decreases beyond 5 km due to scattering and mode conversion of the refracted P-wave by the shallowing interface. The predominant body wave arrivals following the P-waves within the basin are refracted S-waves. These are clear in the steep flank case (Fig. 2-10a), but are complicated by mode conversions in the other basins. In the magnified seismograms for the steep and echelon faulted basins (Fig. 2-10a,b), the refracted S-waves are seen to reflect very weak Rayleigh waves back into the basin from the edge.

The body wave phases outside the basins are due to bedrock refractions, interface edge diffractions and mode conversions at the basin edge. The first arrival beyond the basins is the refracted P-wave. The refracted S-wave is the next significant arrival and achieves its highest amplitude for the steep flanked basin and is less pronounced for the echelon faulted basin, caused in part by the interference of edge diffracted waves. For the dipping flank case, the refracted S-wave is very weak, probably because of weaker P- to S-mode conversion on the sloping interface.

The surface wave phases transmitted outside the basin are caused principally by mode conversions at the basin edges. These may be body to surface or surface to surface conversions. The strongest surface wave is the direct conversion (surface to surface), as was the case for the piecewise constant velocity model. In the present case, however, there are significant conversions from S-waves to surface waves at the basin edge. These can be seen in the magnified seismograms as the weak phases preceding the direct Rayleigh wave phase and parallel to it. They are most coherent for the dipping flank (Fig. 2-10c), probably caused by multiple reflection and conversions of the body waves as they reverberate up the smooth slope. This mechanism is described in a previous study, Wojcik et al. (1981). Conversions from P-waves to Rayleigh waves are not indicated by the seismograms. Any conversion of surface waves is obscured by the transmitted surface wave due to the low frequency resolution of the model.

2.9 Basins With Tangential Surface Traction

The previous seismograms were calculated for a normal surface traction at the origin. Synthetics resulting from a tangential surface traction are illustrated in Fig. 2-11 for the three basins with velocity gradients described above. They again show vertical velocity seismograms normalized by the Rayleigh wave amplitude 300 m from the basin centerline (second seismogram). On the centerline the vertical velocity is zero. The principal Rayleigh wave reflects and transmits from the three basin edges, as described above in Section 2.8, but the body waves and mode converted Rayleigh waves are significantly different, both inside and outside.

Within the basin, P-waves appear as before but, as would be expected, the S-wave phase is clearly stronger. This is difficult to quantify from the

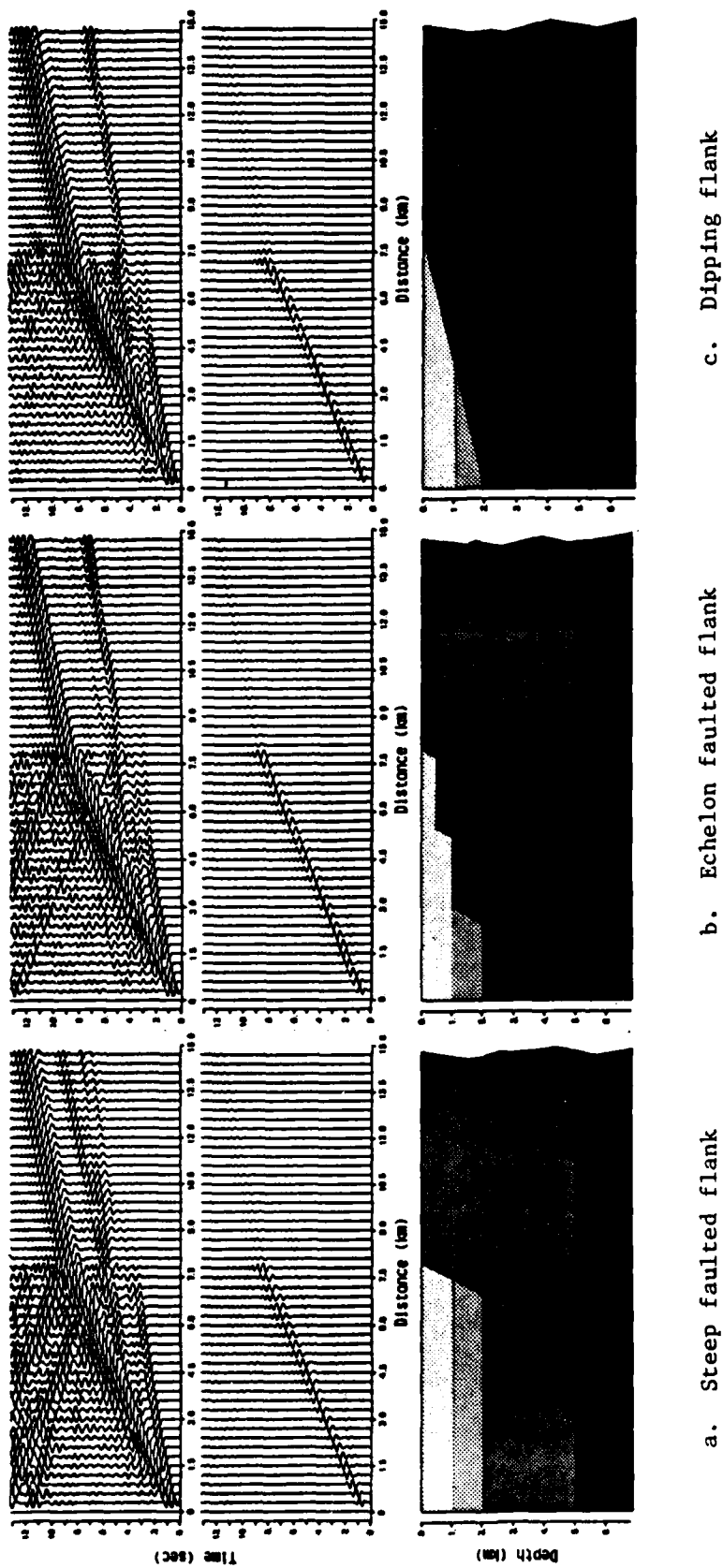


Figure 2-11. Vertical velocity seismograms for the piecewise linear velocity models with tangential surface traction.

seismograms but is evident from relative amplitudes of the converted Rayleigh wave (S-wave to Rayleigh wave) reflected back into the basin. This is seen clearly in magnified seismograms for the steep flanked basin, Fig. 2-11a, and is also in evidence for the echelon faulted flank. The converted Rayleigh wave is completely absent for the dipping flank. There does not appear to be a reflected S-wave in the basin in any case, probably because multiples within the basin tend to obscure weak phases.

The principal difference between normal and tangential sources appears to be body wave and converted phases outside the basin. For the steep flanked basin, Fig. 2-11a, the S-wave from the interior converts to a Rayleigh wave and a weaker, somewhat incoherent S-wave in the exterior. In contrast, for the echelon faulted and dipping flanks, Fig. 2-11b,c, the interior S-wave is transmitted as an S-wave, with little conversion to Rayleigh waves. These transmitted S-waves are virtually nonexistent in the case of normal tractions. Of course, a direct comparison of amplitudes between normal and tangential traction synthetics is not valid because of different normalizations. However, relative scaling of S-wave to P-wave amplitudes in each case confirm that the tangential source excites much higher amplitude S-waves outside the basin for echelon faulted and dipping flanks. Reasons for these differences probably involve diffractions and constructive interference of multiple arrivals outside the basin. Detailed analysis is beyond the scope of the present study.

2.10 The Basin-Range-Basin Model

The previous finite element calculations and interpretations serve to characterize a variety of basin interfaces, velocity functions and source types for a single symmetric basin in a halfspace. In this section, these results are extended to a two-basin model with an intervening 1 km mountain.

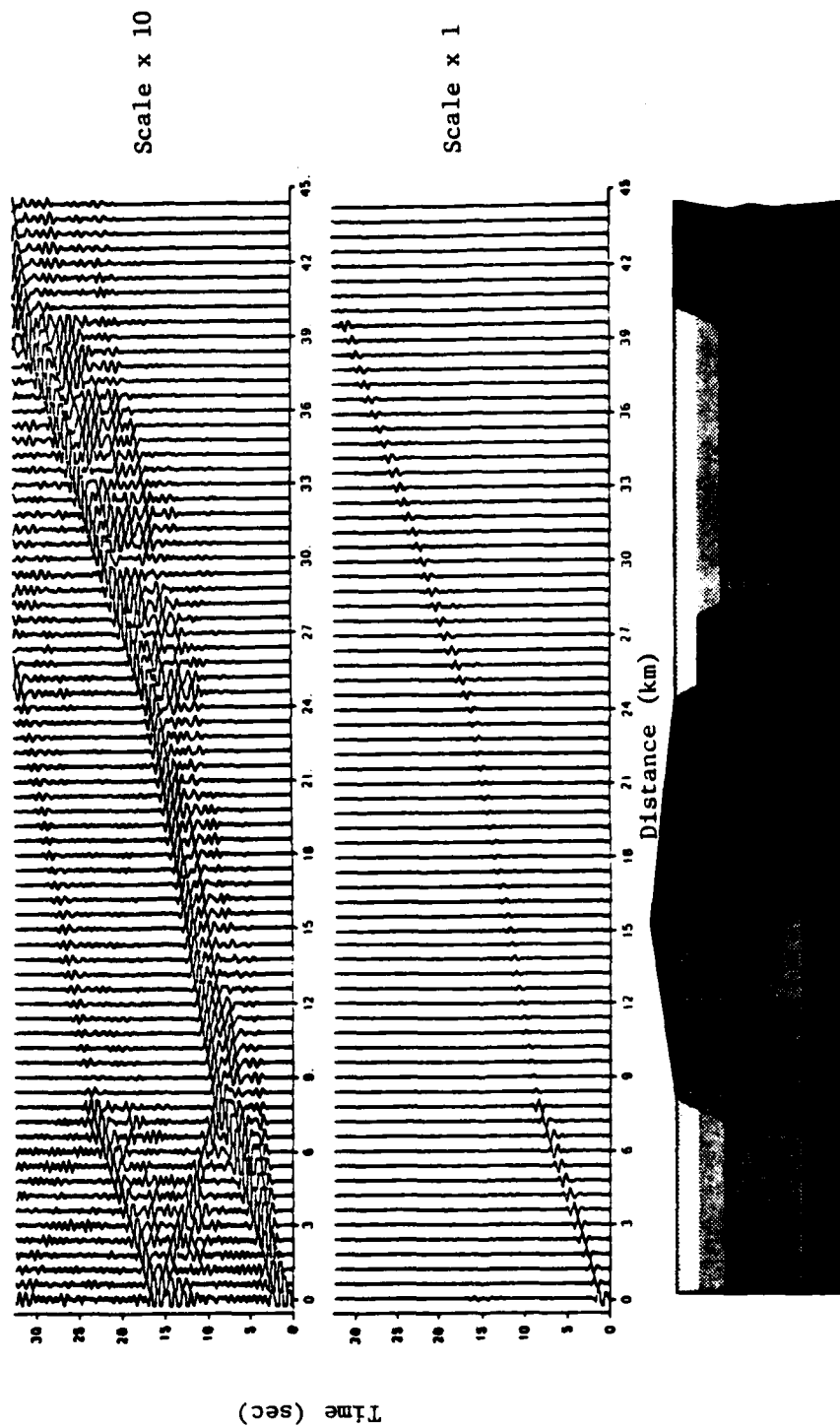


Figure 2-12. Vertical velocity seismograms for the basin-range-basin model with piecewise linear velocity and normal surface traction.

Vertical velocity synthetic seismograms are drawn in Fig. 2-12 for the normal surface traction source. The wavelet frequency is centered at 1 Hz in these synthetics to minimize data storage requirements (rather than the 2 Hz wavelet used previously). Amplitudes are normalized by the Rayleigh wave maximum on the second trace, 600 m from the model centerline where the load is applied.

Qualitative features of the seismograms are as expected from the previous basin flank synthetics. The principal phase is the Rayleigh wave which is partially reflected and transmitted across the first basin edge. The transmitted surface wave travels over the mountain with a decreased amplitude, due to scattering losses and a higher characteristic impedance, and is transmitted with little evidence of reflection into and across the second basin. Although these plane strain results indicate virtually no change in amplitude with distance (except at edges), in actuality, for a point source the Rayleigh wave signal would decay more like $\sqrt{.6/R}$ assuming axisymmetric geometry, where R is distance from the centerline in kilometers. This is, of course, due to cylindrical divergence of the surface wave (assuming unit amplitude at .6 km). Thus, at the mountain peak (R = 16 km), the amplitude is about 20 percent of that shown, and in the center of the second basin (R = 32 km), it is reduced to nearly 14 percent. These are estimates of qualitative behavior only. A three-dimensional calculation is necessary to quantify the true amplitude decay.

Within the first basin, the Rayleigh wave is seen to undergo multiple reverberations, equivalent to reflections from the opposite basin edge. The second reflection at 23 seconds and 8 km in the magnified synthetics is weak and loses coherence in the background noise; however, the transmitted wave is still significant. Over the mountain, the direct Rayleigh wave appears to be only slightly modified by the topography and is followed 15 seconds later by the

much weaker transmitted wave from the reverberation in the basin. In the second basin, the direct wave transmits across the left edge with an increased amplitude because of the decrease in impedance. There is no coherent indication of direct Rayleigh wave reflection at the basin edge. This is probably characteristic of incidence from a high impedance to low impedance medium, but also depends on details of the edge geometry. Across the second basin, the direct wave propagates uniformly.

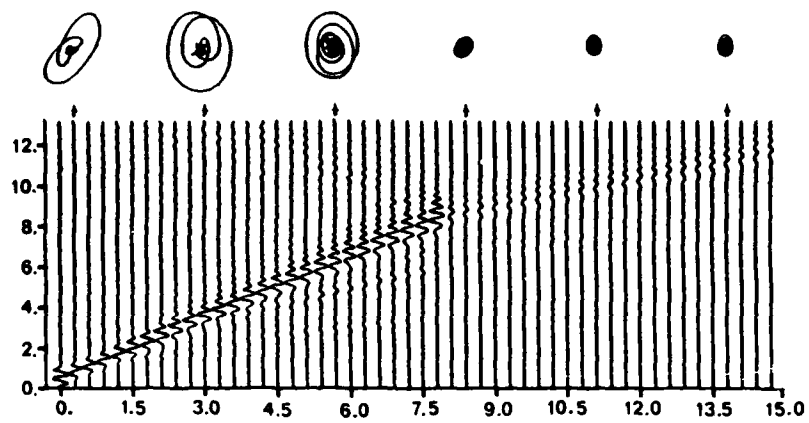
Body wave phases over the left basin and mountain are essentially the same as those found in the steep flanked basin calculation, Fig. 2-10a, with allowance made for the reduced frequency resolution of the present synthetics. Arrivals on the mountain consist of refracted P- and S-waves, a mode converted Rayleigh wave from S-waves in the left basin, and the direct Rayleigh wave. In contrast, over the second basin the body wave arrivals become considerably more involved. Because the velocity gradient goes to zero at a depth of 5 km, the second basin is probably in a shadow for refracted P- and S-waves through the bedrock. Therefore, the first body wave arrivals are shallower refractions, reflected one or more times from the free surface. From the magnified synthetics, the first (refracted) P-wave is seen to decay very rapidly across the basin. Subsequent body wave arrivals are much stronger and appear to correlate with S-wave and Rayleigh wave arrivals at the left edge. That is, they are caused by diffraction and mode conversion from interaction with the faulted flank on the left side of the basin. It is obvious from the seismograms that to understand the complex of arrivals in the second basin requires both higher frequency resolution and a detailed ray theory analysis to discriminate the body and surface waves.

2.11 Selected Particle Motion Plots

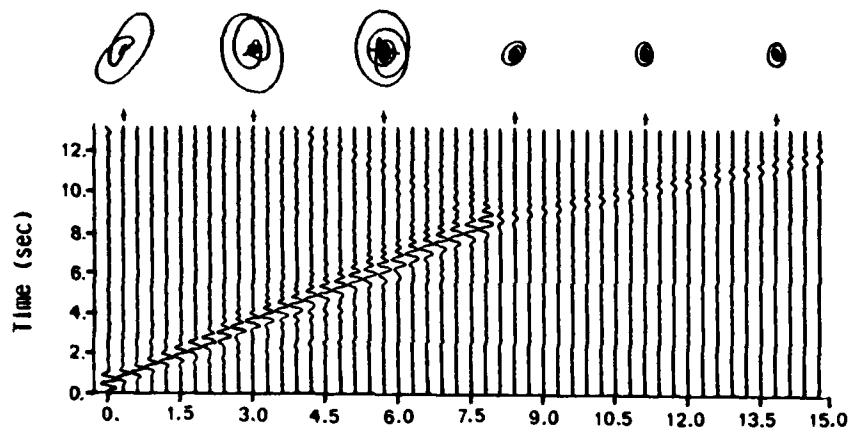
To facilitate comparison of surface wave amplitudes across each model, as well as between models, particle motion plots are drawn above selected seismograms in Figs. 2-13,14,15. They generally show retrograde elliptical orbits corresponding to the Rayleigh wave, and complicated low amplitude motion from the body waves.

In Fig. 2-13, seismograms and orbits are shown for the three basin types with velocity gradients and normal traction source (described in Section 2.9). The most striking feature is the similarity of orbital motion between each basin type. This suggests that the Rayleigh wave is relatively insensitive to details of interface geometry. Wavelength of the 2 Hz surface waves in the basin is on the order of a kilometer, indicating that the depth of significant motion is about 2 km. Therefore, in the deeper basin interior away from the edges, similar orbits would be expected. However, the plots show that this is true near the edges as well, indicating the insensitivity of free surface Rayleigh waves (in contrast to ducted Rayleigh waves) to the interface shapes and impedance contrasts assumed here.

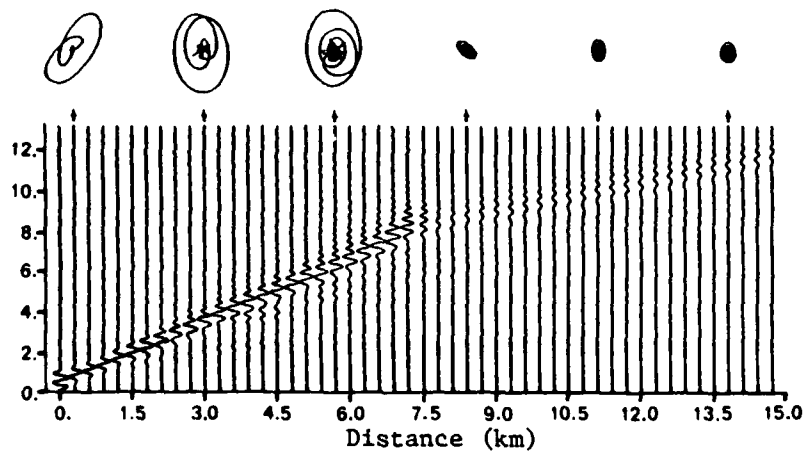
Orbits outside the three basins also show that the transmitted surface wave amplitude is relatively independent of the edge geometry, although the details of motion appear to differ more than in the interior. The maximum amplitude ratio of interior to exterior waves is approximately a factor of three in all cases. The ellipticity (ratio of vertical to horizontal motion) is generally about 1.5. Major axes of the elliptical orbits are vertical, except near the traction source and very close to the basin edge. Near the source, the orbit is skewed because strong body waves are superposed on the surface wave. However, close to the edge the skewness is probably caused by the local



a. Steep faulted flank



b. Echelon faulted flank



c. Dipping flank

Figure 2-13. Particle motion plots for the three basin types with velocity gradients and normal surface traction.

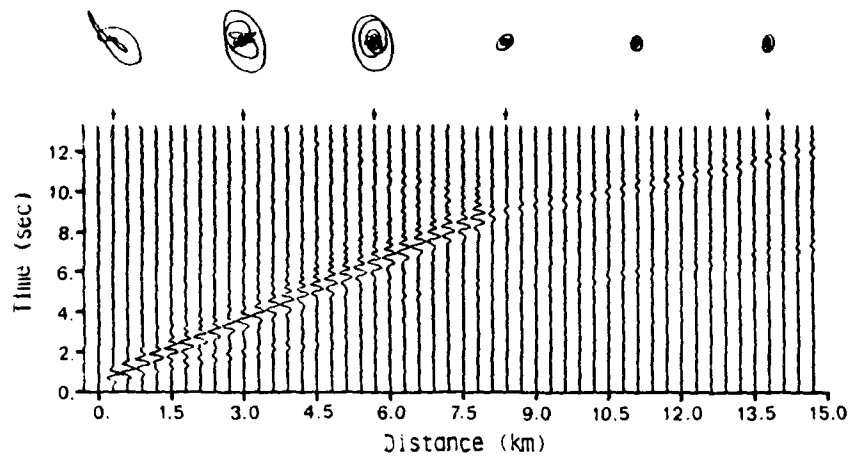


Figure 2-14. Particle motion plots for tangential surface traction on the echelon faulted flank.

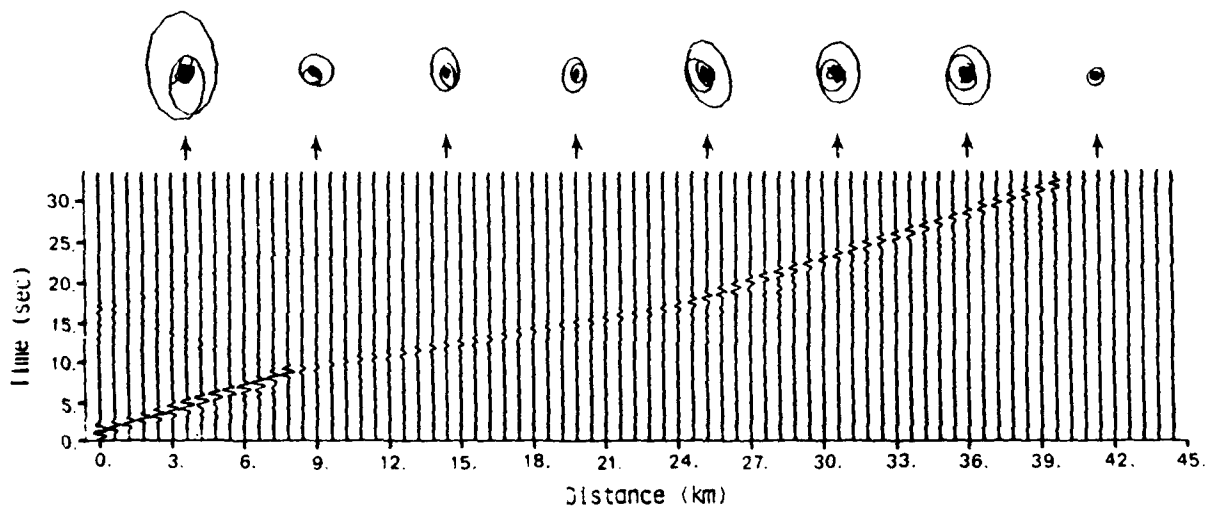


Figure 2-15. Particle motion plots for the basin-range-basin model with normal surface traction.

change in wavespeed in the horizontal direction, similar to the effect of anisotropy.

Particle motions from the tangential traction source are plotted for the echelon faulted basin in Fig. 2-14. They show a more erratic motion in the first two orbital plots (compared to the same basin in Fig. 2-13) because of stronger refracted body waves from the tangential source. The ellipticity is found to be in the range 1.4-1.5 and the maximum amplitude ratio of interior to exterior waves is again about three because the Rayleigh wave, once generated, is independent of source type.

In Fig. 2-15, particle motion is plotted for the basin-range-basin model. Comparing amplitude in the left basin to that over the mountain gives a ratio of approximately three, although there appears to be some variability over the mountain. The amplitude ratio between left and right basins is about 1.7. As for any of these plane strain models, the amplitude ratios should be scaled to account for the Rayleigh wave's cylindrical divergence from a more realistic point source.

SECTION 3

THE FULL WAVE FIELD SOLVER

This section describes the discrete numerical algorithm used to solve the time domain wave field equations in two-dimensional inhomogeneous, elastic and acoustic media. The physical domain is a rectangular 2-D section over which the Lagrangian, small displacement computational mesh is globally cartesian. A discrete system of equations is derived by factoring the wave field into elastic and inertial components and discretizing each separately. A finite element displacement approximation over rectangular mesh boxes (elements) yields elastic force resultants at the mesh points (nodes), while a lumped mass approximation at the mesh points provides the inertial force resultants. The nodal distribution of lumped masses (particles) is moved incrementally in time according to the discrete impulse-momentum equality, with the incremental elastic restoring forces at each node accumulated from contiguous elements. The global time increment is chosen smaller than the shortest transit time across any element, yielding a stable explicit integration algorithm for the uncoupled system of discrete equations. Large-scale modeling applications require on the order of 10^5 nodes entailing approximately 10^{10} floating point operations per model. Therefore, coding of the algorithm is necessarily designed for the pipeline and parallel capabilities of existing supercomputers, specifically, vectorization on the CRAY-1.

3.1 Background

Solution techniques for the full elastic/acoustic wave field in inhomogeneous media generally depend on some form of discrete algorithm. The usual basis is a finite difference (FD) or finite element (FE) spatial discretization over an appropriate computational mesh. In the case of finite differences, the governing partial differential equations (PDE's) are typically reduced

to a discrete system of ordinary differential equations (ODE's) in time by means of difference operators for spatial derivatives at mesh points. In contrast, with finite elements the particle displacement field is discretized via element shape functions, and the reduced system of discrete nodal ODE's derived by enforcing element equilibrium. Provided the differencing operator and element shape function are of the same order, both FD and FE discretizations result in similar systems to be solved, e.g., Frazier et al. (1973). Note that the FE method does not explicitly use the governing PDE's (as does the FD method) but instead satisfies equilibrium directly. In this sense it provides a more fundamental algorithm, based directly on elemental mechanics rather than infinitesimal mathematics (which are abstracted from the mechanics). This is best appreciated in terms of ease of implementation for complicated media and shapes, as well as the simplicity of elemental solutions and higher order generalizations.

There remains time integration of the discrete field equations by means of implicit and/or explicit schemes, whereby the ODE's are reduced to an algebraic system. These equations may be classified as hyperbolic (wave-like) and/or elliptic (potential-like) depending on the time scales and characteristic lengths in the problem. The terms, hyperbolic-elliptic, follow from the usual classification of partial differential equations. Briefly, for elastic/acoustic fields, when inertial forces dominate elastic forces, the system is hyperbolic--but when elastic forces dominate, it is elliptic. In a hyperbolic system, disturbances at one point do not influence other points until the wave arrives. However, in an elliptic system, a disturbance at any point influences every other point without time delay. Explicit and implicit time integrators exhibit similar behavior. Explicit schemes (hyperbolic integrators) involve the independent integration of each nodal equation of motion by

virtue of the hyperbolicity of the problem. That is, the time step is chosen small enough that integration (motion) of one node does not influence an adjacent node during one time step. Implicit schemes (elliptic integrators) require the simultaneous integration of the entire system of equations, assuming coupling between all nodes over one time step, i.e., elliptic behavior. This allows the use of a somewhat larger time step than for the explicit case. Actually all nodes are not coupled in hyperbolic problems, but depend on each node's sphere of influence, proportional to the time step chosen; hence, only those within the sphere are coupled in an implicit scheme. This feature makes an implicit solver for large hyperbolic systems prohibitively redundant.

In the present study, time domain wave propagation of pulses is the phenomenon of interest, governed by hyperbolic equations. Because the requirement is to solve very large systems at fast cycling rates (mesh or element time steps/second), explicit time integration of the discrete equations is essential. The choice of spatial discretization, finite element or finite difference, is not so obvious in view of the inherent similarities of the resulting systems. However, experience with the implementation of both methods shows that the intuitive and mechanical aspects of finite element modeling offer clear advantages. Therefore, an explicit finite element algorithm is used here, and is described in the remainder of this section.

3.2 Computational Mesh

The first consideration in implementing a large-scale vectorized wave solver is the computational mesh--i.e., the distribution of discrete field points through the domain. Given a rule for field interpolation between points, the mesh must be capable of resolving the wave pulse in space and time, as well as inhomogeneities in the medium. In this study it must also satisfy a large-scale requirement--that the minimum wavelength resolved be a

small fraction (rather than a multiple) of the characteristic dimension of the model. On one computational side, the mesh must possess sufficient regularity to permit vectorization of the algorithm and minimize the arithmetic and storage used in coordinate processing. Finally, with regard to physical modeling, it should easily represent (from a user's viewpoint) complicated inhomogeneities and interfaces to a degree of approximation consistent with its frequency resolution.

The simplest computational mesh satisfying these requirements is cartesian, illustrated in Fig. 3-1 for equidistant grid lines. The bold contours are a fit of the geologic model in Fig. 2-1 showing the stepwise resolution of material interfaces. In applications, the grid density necessary for pulse resolution would be at least quadrupled, with sixteen times more elements--approximately 36,000 in Fig. 3-1--yielding a dense matrix of (picture) elements for inhomogeneous modeling. This identification of finite elements with picture elements, so-called pixels in incremental computer graphics applications, e.g., Newman and Sproull (1979), provides a simple, flexible scheme for constructing large-scale models while minimizing user and computational overhead.

To propagate a wave pulse through the inhomogeneous grid, some minimum number of elements must support it, depending on the degree of field interpolation function used. An adequate minimum in what follows is ten per wavelength of the highest frequency component to be preserved in the pulse. Therefore, if an interface in the cartesian grid is composed of one or two element steps as in Fig. 3-1 (typically), its local scale is equal to or less than one-fifth of the shortest wavelength. A somewhat denser support of the wave over the mesh, in conjunction with inherent smoothing by the lumped mass and finite element discretizations, makes the interface practically negligible in terms of its non-specular scattering effect on pulses.

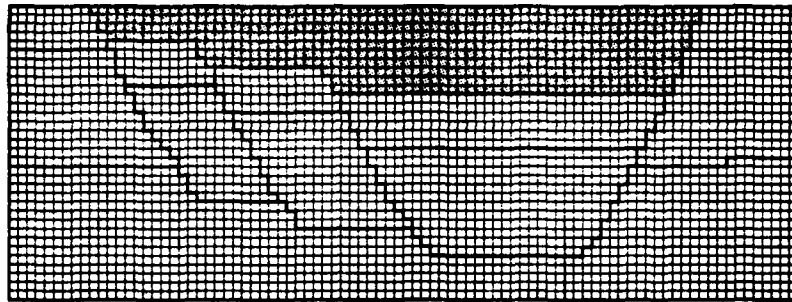


Figure 3-1. Example of a cartesian mesh with equidistant grid lines, and the stepwise resolution of geology (c.f. Fig. 2-1).

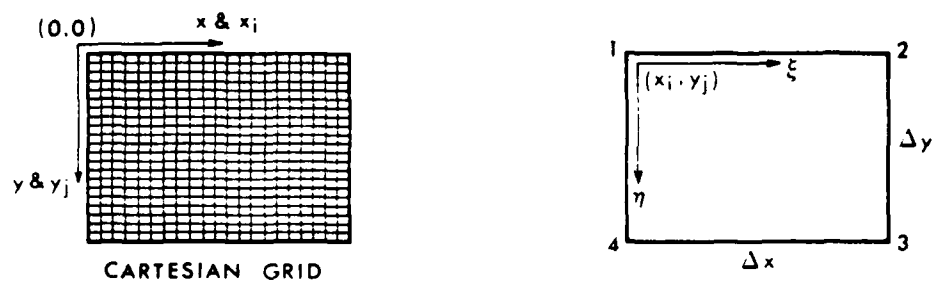


Figure 3-2. Cartesian grid and element coordinate systems.

Alternatively, the stepwise interface roughness could be reduced by using conforming elements, e.g., quadrilaterals for a piecewise linear fit. However, this increases arithmetic, storage and the level of element approximation, as well as complicating the vectorization of code loops necessary for rapid mesh cycling. For these reasons the simple cartesian mesh with stepwise resolution of inhomogeneities will be used exclusively in what follows.

3.3 The Finite Element Approximation

To introduce finite element discretizations of the wave field, consider a rectangular domain covered by a cartesian grid of rectangular elements. Global coordinates are (x,y) and local (element) coordinates are (ξ,η) , measured from the origin at (x_i, y_j) of the ij element. These are illustrated in Fig. 3-2. Assuming that the material displacement vector, $\underline{d}(x,y,t) = (u,v)^T$ is regular over the grid, it may be expanded in a two-dimensional time dependent Taylor series about any of the local origins as

$$\begin{aligned} \underline{d}(x_i + \xi, y_j + \eta, t) = & \underline{d}(x_i, y_j, t) + \xi \underline{d}_{x_i} + \eta \underline{d}_{y_j} \\ & + \frac{1}{2} (\xi^2 \underline{d}_{x_i x_i} + 2\xi\eta \underline{d}_{x_i y_j} + \eta^2 \underline{d}_{y_j y_j}) + \dots \end{aligned} \quad (3-1)$$

where $0 \leq \xi \leq \Delta x$, $0 \leq \eta \leq \Delta y$ and derivatives at the grid points are denoted by subscripts, e.g., \underline{d}_{x_i} . When the grid spacing is made sufficiently small (but finite), only certain leading terms in this expansion will be significant within the element. If these principal degrees of freedom can be solved in terms of nodal displacements, i.e., the generalized displacement of the problem, then local continuum analysis may proceed on this basis. Provided the series truncation is uniform over the grid of local expansions, the global field is continuous, C^0 , i.e., inter-element displacements are compatible.

The simplest local interpolant is a two-dimensional version of the familiar trapezoidal rule, which follows by neglecting curvature terms, i.e., second and higher x_i and y_i derivatives in (3-1), giving

$$d(x_i + \xi, y_j + \eta, t) \approx d(x_i, y_j, t) + \xi d_{x_i} + \eta d_{y_j} + \xi \eta d_{x_i y_j} \quad (3-2)$$

For this truncation of the Taylor series the remaining nodal derivatives are expressible as first order differences of the element nodal displacements,

$$\underline{\delta}_n(t) = (u_n, v_n)^T \text{ as}$$

$$d_{x_i} \approx (\delta_2 - \delta_1) / \Delta x, \quad d_{y_j} \approx (\delta_4 - \delta_1) / \Delta y, \quad d_{x_i y_j} \approx (\delta_1 - \delta_2 + \delta_3 - \delta_4) / \Delta x \Delta y \quad (3-3)$$

where n runs from 1 to 4 (clockwise in Fig. 3-2). Introducing the nodal displacement vector,

$$\underline{\delta}_e \equiv (\underline{u}, \underline{v})^T = (u_1, u_2, u_3, u_4, v_1, v_2, v_3, v_4)^T$$

the element expansion, (3-2) becomes,

$$d(x_i + \xi, y_j + \eta, t) \approx D_e(\xi, \eta) \underline{\delta}_e \quad (3-4)$$

where

$$D_e = \frac{1}{\Delta x \Delta y} \begin{pmatrix} \bar{\xi} \bar{\eta} & \bar{\xi} \bar{\eta} & \bar{\xi} \eta & \bar{\xi} \eta & 0 & 0 & 0 & 0 \\ 0 & 0 & 0 & 0 & \bar{\xi} \eta & \bar{\xi} \bar{\eta} & \xi \eta & \xi \bar{\eta} \end{pmatrix}$$

and

$$\bar{\xi} \equiv \Delta x - \xi, \quad \bar{\eta} \equiv \Delta y - \eta.$$

Retention of higher order derivatives in the truncation requires additional data at intermediate points on or in the element for a unique representation. In view of the minimal arithmetic involved in (3-4) and proven utility of the trapezoidal rule in numerical analysis, higher order elements will not be considered further.

With an approximation (interpolant) available for intra-element displacements, 2-D elasticity theory yields elemental stresses and strains. The linear, isotropic stress-strain relation is

$$\sigma \equiv (\sigma_{\xi\xi}, \sigma_{\eta\eta}, \sigma_{\xi\eta})^T = C \epsilon, \quad (3-5)$$

where the infinitesimal strains are

$$\epsilon \equiv (\epsilon_{\xi\xi}, \epsilon_{\eta\eta}, \epsilon_{\xi\eta})^T = (u_{\xi}, v_{\eta}, u_{\eta} + v_{\xi})^T, \quad (3-6)$$

C is the constitutive matrix given by

$$C \equiv c_1 \begin{pmatrix} 1 & c_2 & 0 \\ c_2 & 1 & 0 \\ 0 & 0 & c_3 \end{pmatrix}, \quad (3-7)$$

and the constants are

$$\text{Plane strain: } c_1 = (3K+4G)/3, \quad c_2 = (3K-2G)/(3K+4G), \quad c_3 = G/c_1$$

$$\text{Plane stress: } c_1 = 4G(3K+G)/(3K+4G), \quad c_2 = (3K-2G)/(3K+G)/2, \quad c_3 = G/c_1$$

with K and G the bulk and shear moduli, respectively. Strains are evaluated by differentiating $d = (u, v)^T$ in (3-4) giving

$$\epsilon = B_e \delta_e \quad (3-8)$$

where B_e is the strain-displacement matrix,

$$B_e = \frac{1}{\Delta x \Delta y} \begin{pmatrix} -\bar{\eta} & \bar{\eta} & \eta & -\eta & 0 & 0 & 0 & 0 \\ 0 & 0 & 0 & 0 & -\bar{\xi} & -\xi & \xi & \bar{\xi} \\ -\bar{\xi} & -\xi & \xi & \bar{\xi} & -\bar{\eta} & \bar{\eta} & \eta & -\eta \end{pmatrix} \quad (3-9)$$

Therefore, from (3-5) and (3-8) the stress-displacement relation is

$$\underline{\sigma} = \underline{CB}_e \underline{\delta}_e. \quad (3-10)$$

The final step is to calculate the generalized elastic and inertial forces, $\underline{f}_e = \underline{f}_e^E + \underline{f}_e^I$, i.e., the equivalent nodal forces corresponding to the generalized displacements, $\underline{\delta}_e$. This is accomplished using the principle of virtual work. For a virtual displacement, $\hat{\underline{\delta}}_e$ of the nodes the internal work is

$$\int_A \hat{\underline{\delta}}_e^T \underline{\sigma} dA = \int_0^{\Delta y} \int_0^{\Delta x} \hat{\underline{\delta}}_e^T \underline{B}_e^T \underline{CB}_e \underline{\delta}_e d\xi d\eta$$

and the external work of the nodal elastic forces is $\hat{\underline{\delta}}_e^T \underline{f}_e^E$. Equating these expressions, noting that $\hat{\underline{\delta}}_e$ is arbitrary, yields

$$\underline{f}_e^E = \underline{K}_e \underline{\delta}_e \quad (3-11)$$

where

$$\underline{K}_e = \int_0^{\Delta y} \int_0^{\Delta x} \underline{B}_e^T \underline{CB}_e d\xi d\eta \quad (3-12)$$

is the element stiffness matrix. Similarly, the work of inertial forces due to constant mass density, ρ is

$$\int_A \hat{\underline{\delta}}_e^T (\rho \underline{\ddot{d}}) dA = \int_0^{\Delta y} \int_0^{\Delta x} \hat{\underline{\delta}}_e^T \underline{D}_e^T \rho \underline{D}_e \underline{\ddot{\delta}}_e d\xi d\eta$$

and that of the corresponding nodal forces is $-\hat{\underline{\delta}}_e^T \underline{f}_e^I$. Equating and solving gives

$$\underline{f}_e^I = -\underline{M}_e \underline{\ddot{\delta}}_e \quad (3-13)$$

where

$$\underline{M}_e = \rho \int_0^{\Delta y} \int_0^{\Delta x} \underline{D}_e^T \underline{D}_e d\xi d\eta \quad (3-14)$$

is the element mass matrix.

The symmetric stiffness and mass matrices are 8 x 8 for 2-D and their closed form calculation from (3-12, 14) is straightforward, involving the integration of simple polynomials over the element. The resulting stiffness matrix is fully populated while the mass matrix consists of two 4 x 4 blocks on the main diagonal. Both are given in Przemieniecki (1968), for example, and a straightforward numerical evaluation of the resulting force equations, (3-11,13) requires approximately 150 floating point operations (adds, multiplies, etc.) per element for \underline{f}_e^E and 50 such operations for \underline{f}_e^I .

The discrete system of equations governing motion of the single finite element follows from D'Alembert's principle (dynamic equilibrium, i.e., $\underline{f}_e^E = \underline{f}_e^I + \underline{g}_e$) as

$$M \ddot{\underline{\delta}}_e = -K \underline{\delta}_e + \underline{g}_e \quad (3-15)$$

The force vector, \underline{g}_e represents influence of adjacent elements, external forces, etc. In order to solve the linear system, it is very useful to transform the equations to a more natural displacement basis than the nodal basis in (3-15).

3.4 The Canonical Finite Element Basis

Element stiffness and inertia properties can be defined with respect to any complete set of displacement modes. These may be nodal displacements as in (3-11), or translations and some combination of element deformations, e.g., extension, shear, dilatation, rotation, etc. Although the cartesian displacement basis used above is ideal for derivation of the governing ODE's, in terms of computational efficiency and an understanding of element dynamics, it is not. The best choice is the canonical finite element basis--defined here to be a displacement basis in which the mass matrix is diagonal (by linear transformation rather than lumped mass approximation). This definition

requires a nontrivial eigenvalue-eigenvector analysis of (3-14) to determine the basis. Alternatively, the canonical basis may be defined by the orthogonal cartesian displacement modes of a continuum element: translations T_x, T_y , and element centered extensions E_x, E_y , shears S_x, S_y , and bends B_x, B_y . These are illustrated in Fig. 3-3. This modal definition yields a convenient mechanical interpretation.

The canonical basis is found most directly by inspection of the modes pictured in Fig. 3-3. Writing the modal vector as

$$\delta_{\sim m} = (T_x, E_x, S_x, B_x, T_y, E_y, S_y, B_y)^T \quad (3-16)$$

the normalized orthogonal transformation, S between nodal and modal basis vectors is

$$\delta_{\sim e} = S \delta_{\sim m} = \frac{1}{2} \begin{pmatrix} S_1 & (0) \\ (0) & S_2 \end{pmatrix} \delta_{\sim m} \quad (3-17)$$

where S is unitary ($S^{-1} = S^T$) and its nonzero blocks are

$$S_1 = \begin{pmatrix} 1 & -1 & -1 & 1 \\ 1 & 1 & -1 & -1 \\ 1 & 1 & 1 & 1 \\ 1 & -1 & 1 & -1 \end{pmatrix}, \quad S_2 = \begin{pmatrix} 1 & -1 & -1 & 1 \\ 1 & -1 & 1 & -1 \\ 1 & 1 & 1 & 1 \\ 1 & 1 & -1 & -1 \end{pmatrix}. \quad (3-18)$$

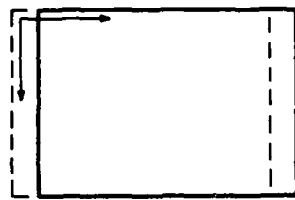
The columns of this transformation constitute the modes (eigenvectors), i.e., the normalized nodal displacements ordered clockwise from the origin in Fig. 3-3. In the new basis, element displacement and stress-strain relations are

$$\tilde{d} = D_e \delta_{\sim e} = D_m \delta_{\sim m} = D_e S \delta_{\sim m}, \quad (3-19)$$

$$\tilde{\epsilon} = B_e \delta_{\sim e} = B_m \delta_{\sim m} = B_e S \delta_{\sim m}, \quad (3-20)$$

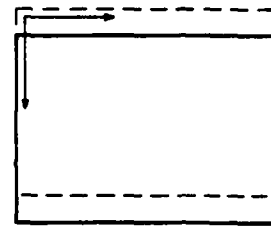
$$\tilde{\sigma} = C \tilde{\epsilon} = D B_e S \delta_{\sim m}. \quad (3-21)$$

Evaluating the modal strain- and stress-displacement matrices, the strain and stress equations are

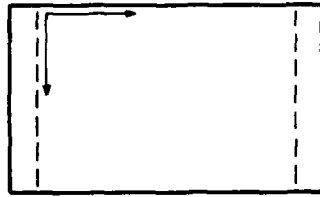


$$T_x: \underline{u} = \frac{1}{2} (1, 1, 1, 1)^T$$

TRANSLATION

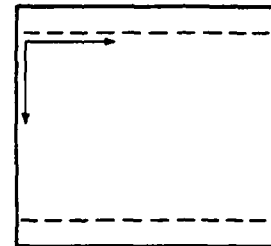


$$T_y: \underline{v} = \frac{1}{2} (1, 1, 1, 1)^T$$

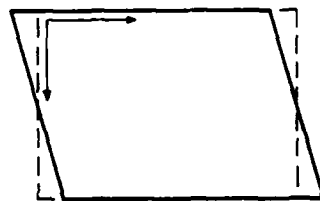


$$E_x: \underline{u} = \frac{1}{2} (-1, 1, 1, -1)^T$$

EXTENSION

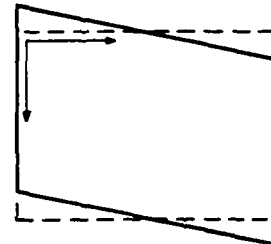


$$E_y: \underline{v} = \frac{1}{2} (-1, -1, 1, 1)^T$$

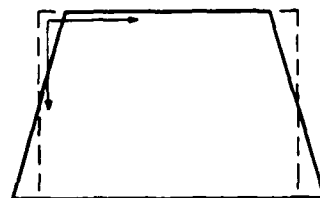


$$S_x: \underline{u} = \frac{1}{2} (-1, -1, 1, 1)^T$$

SHEAR

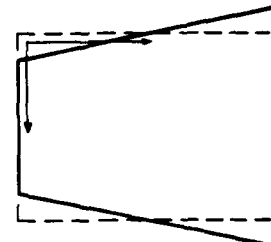


$$S_y: \underline{v} = \frac{1}{2} (-1, 1, 1, -1)^T$$



$$B_x: \underline{u} = \frac{1}{2} (1, -1, 1, -1)^T$$

BEND



$$B_y: \underline{v} = \frac{1}{2} (1, -1, 1, -1)^T$$

Figure 3-3. The normalized orthogonal cartesian displacement modes of a 2-D continuum element.

$$\begin{pmatrix} \epsilon_{\xi\xi} \\ \epsilon_{\eta\eta} \\ \epsilon_{\xi\eta} \end{pmatrix} = \frac{1}{4\Delta x\Delta y} \begin{pmatrix} 0 & \Delta y & 0 & 2\eta-\Delta y & 0 & 0 & 0 & 0 \\ 0 & 0 & 0 & 0 & 0 & \Delta x & 0 & 2\xi-\Delta x \\ 0 & 0 & \Delta x & 2\xi-\Delta x & 0 & 0 & \Delta y & 2\eta-\Delta y \end{pmatrix} \delta_m, \quad (3-22)$$

$$\begin{pmatrix} \sigma_{\xi\xi} \\ \sigma_{\eta\eta} \\ \sigma_{\xi\eta} \end{pmatrix} = \frac{1}{4\Delta x\Delta y} \begin{pmatrix} 0 & \Delta y & 0 & 2\eta-\Delta y & 0 & c_2\Delta x & 0 & c_2(2\xi-\Delta x) \\ 0 & c_2\Delta y & 0 & c_2(2\eta-\Delta y) & 0 & \Delta x & 0 & 2\xi-\Delta x \\ 0 & 0 & c_3\Delta x & c_3(2\xi-\Delta x) & 0 & 0 & c_3\Delta y & c_3(2\eta-\Delta y) \end{pmatrix} \delta_m, \quad (3-23)$$

which demonstrates that translation (columns 1 and 5) makes no contribution to the stress-strain state, while extension (columns 2 and 6) and shear (3 and 7) produce uniform states over the element, and bending (4 and 8) adds linear variation.

To express the stiffness and inertia matrices, $K_m = \int_A B_m^T C B_m dA$ and $M_m = \rho \int_A D_m^T D_m dA$ respectively; in the new basis it is only necessary to set $B_m = B_e S$ and $D_m = D_e S$ and evaluate the integrals, giving

$$K_m = S^T K_e S = \frac{c_1}{4} \begin{pmatrix} 0 & 0 & 0 & 0 & 0 & 0 & 0 & 0 \\ 0 & a_1 & 0 & 0 & 0 & c_2 & 0 & 0 \\ 0 & 0 & a_2 c_3 & 0 & 0 & 0 & c_3 & 0 \\ 0 & 0 & 0 & b_1 & 0 & 0 & 0 & 0 \\ 0 & 0 & 0 & 0 & 0 & 0 & 0 & 0 \\ 0 & c_2 & 0 & 0 & 0 & a_2 & 0 & 0 \\ 0 & 0 & c_3 & 0 & 0 & 0 & a_1 c_3 & 0 \\ 0 & 0 & 0 & 0 & 0 & 0 & 0 & b_2 \end{pmatrix}, \quad (3-24)$$

$$M_m = S^T M_e S = m \begin{pmatrix} 1 & 0 & 0 & 0 & 0 & 0 & 0 & 0 \\ 0 & 1/3 & 0 & 0 & 0 & 0 & 0 & 0 \\ 0 & 0 & 1/3 & 0 & 0 & 0 & 0 & 0 \\ 0 & 0 & 0 & 1/9 & 0 & 0 & 0 & 0 \\ 0 & 0 & 0 & 0 & 1 & 0 & 0 & 0 \\ 0 & 0 & 0 & 0 & 0 & 1/3 & 0 & 0 \\ 0 & 0 & 0 & 0 & 0 & 0 & 1/3 & 0 \\ 0 & 0 & 0 & 0 & 0 & 0 & 0 & 1/9 \end{pmatrix}, \quad (3-25)$$

where $m \equiv \rho \Delta x \Delta y$ is the element mass and $a_1 \equiv \Delta y / \Delta x$, $a_2 \equiv \Delta x / \Delta y$, $b_1 = (a_1 + a_2 c_3) / 3$, $b_2 = (a_2 + a_1 c_3) / 3$. This demonstrates that the canonical basis does indeed diagonalize the mass matrix, as well as significantly reducing the number of nonzero entries in the stiffness matrix (from 69 to 10) due to the simple modal stress states.

3.5 Canonical Element Dynamics

In the canonical basis the ODE's governing element dynamics become

$$M_{m \sim m} \ddot{\delta}_{m \sim m} = -K_{m \sim m} \delta_{m \sim m} + g_m \quad (3-26)$$

With M_m diagonal and K_m sparse, this representation allows closed form solutions. In particular, the homogeneous system (setting $g_m = 0$) reduces to the following set of equations for the element centered free-vibration modes,

$$\begin{aligned} \begin{pmatrix} \ddot{E}x \\ \ddot{E}y \end{pmatrix} &= \frac{-3c_1}{4m} \begin{pmatrix} a_1 & c_2 \\ c_2 & a_2 \end{pmatrix} \begin{pmatrix} E x \\ E y \end{pmatrix}, \\ \begin{pmatrix} \ddot{S}x \\ \ddot{S}y \end{pmatrix} &= \frac{-3c_1 c_3}{4m} \begin{pmatrix} a_2 & 1 \\ 1 & a_1 \end{pmatrix} \begin{pmatrix} S x \\ S y \end{pmatrix}, \\ \begin{pmatrix} \ddot{B}x \\ \ddot{B}y \end{pmatrix} &= \frac{-9c_1}{4m} \begin{pmatrix} b_1 & 0 \\ 0 & b_2 \end{pmatrix} \begin{pmatrix} B x \\ B y \end{pmatrix}, \end{aligned} \quad (3-27)$$

where only the bending modes are uncoupled. Assuming time harmonic solutions, i.e., $ae^{i\omega t}$ and solving for the unknown frequencies and modal coupling,

Extensional vibrations

$$\begin{aligned}\omega_{Ex} = \omega_{Ey} &= \frac{1}{2} \sqrt{(3c_1/2m)(a_1+a_2 \pm \sqrt{(a_1-a_2)^2 + 4c_2^2})} \\ Ey/Ex &= (a_2-a_1 \pm \sqrt{(a_1-a_2)^2 + 4c_2^2}) / (2c_2)\end{aligned}\quad (3-28)$$

Shearing vibrations

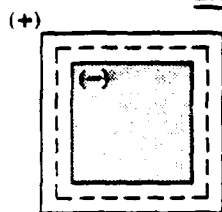
$$\omega_{Sx} = \omega_{Sy} = \begin{cases} 0 ; Sy/Sx = -a_2 \\ \frac{1}{2} \sqrt{(3G/m)(a_1+a_2)} ; Sy/Sx = a_1 \end{cases} \quad (3-29)$$

Bending vibrations

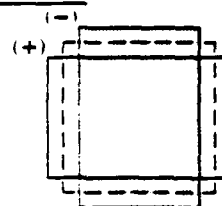
$$\omega_{Bx} = \frac{3}{2} \sqrt{c_1 b_1 / m} , \quad \omega_{By} = \frac{3}{2} \sqrt{c_1 b_2 / m} \quad (3-30)$$

Specializing these solutions to a square element ($\Delta x = \Delta y$, hence $a_1 = a_2 = 1$, $b_1 = b_2 = (1+c_3)/3$) yields the simple picture of free element dynamics shown in Fig. 3-4. The zero frequency shearing vibration, $Sy/Sx = -1$, is seen to yield rigid body rotation, hence there are only five deformational modes. The pure shear mode, $Sy/Sx = 1$ and pull-push extensional mode, $Ey/Ex = -1$ have the lowest natural frequency, $\omega_N \equiv \sqrt{3/2} c_s / \Delta x$; while the bending modes, Bx and By and the pull-pull extensional mode, $Ey/Ex = 1$ have the highest, $\omega_{Bx} = \sqrt{(k^2+1)/2} \omega_N$ and $\omega_{Ex} = \sqrt{k^2-1} \omega_N$ ($\omega_{Ex} > \omega_{Bx}$ when $k > \sqrt{2}$), where $k \equiv c_p/c_s$ is the wavespeed ratio. When $c_s = 0$ ($k \rightarrow \infty$) in an acoustic medium these natural frequencies reduce to $\omega_N = 0$, $\omega_{Bx} = \sqrt{3/2} c_p / \Delta x$ and $\omega_{Ex} = \sqrt{3/2} c_p / \Delta x$. The natural period, $T_N = 2\pi/\omega_N$ may be written as $T_N \approx 5.13k \Delta x / c_p$. In geologic media for example, where $k = \sqrt{3}$ is a good approximation, the natural element period is $T_N \approx 8.89 \Delta t_e$, with Δt_e denoting P-wave transit time across the element. Thus, in applications ω_N is a clear upper bound to the frequency resolution of a finite element mesh based on this element. In operation, if the mesh is driven externally at frequencies approaching or exceeding ω_N ,

EXTENSIONAL VIBRATIONS

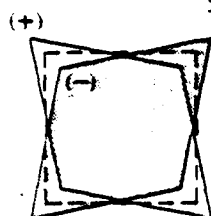


$$E_1: \Omega = \sqrt{k^2 - 1}, E_y/E_x = 1$$

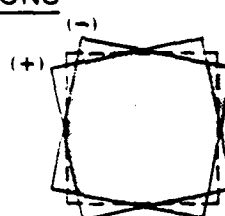


$$E_2: \Omega = 1, E_y/E_x = -1$$

SHEARING VIBRATIONS

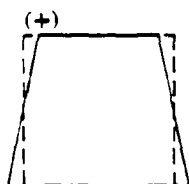


$$S_2: \Omega = 1, S_y/S_x = 1$$

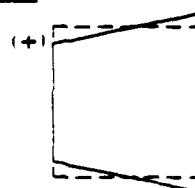


$$S_1: \Omega = 0, S_y/S_x = -1$$

BENDING VIBRATIONS



$$B_x: \Omega = \sqrt{\frac{k^2 + 1}{2}}, B_x \propto e^{i\omega t}$$



$$B_y: \Omega = \sqrt{\frac{k^2 + 1}{2}}, B_y \propto e^{i\omega t}$$

Figure 3-4. Free vibration modes and frequencies in the canonical finite element basis. The reduced frequency is $\Omega \equiv \sqrt{2/3} \omega \Delta x / c_s$ and the signs at node 1 correspond to those of the x component mode assumed in Fig. 3-3. The wavespeed ratio, c_p/c_s , is denoted by k .

individual elements will resonate at their modal frequencies, introducing a spurious high frequency ringing to the wave field. This is, of course, equivalent to the numerical dispersion generally associated with discrete mathematical systems or the ringing of any mechanical (force-motion) transducer.

3.6 Explicit Integration and the Lumped Mass Approximation

With the element ODE's known, the equations must be assembled (coupled) and solved by numerical integration in time, specifically by advancing the global system incrementally, at timestep Δt . However, the degree of system coupling depends on the extent of dynamic interaction between nodes during a single timestep. This is measured by the radius of a node's circle of influence (sonic circle), $r = c_p t$ shown graphically in Fig. 3-5. If Δt is less than the shortest element transit time, i.e., if the circle is contained within a quad of elements (the smallest circle in Fig. 3-5), then no global interaction occurs because all nodal motions are uncoupled during one timestep. Such behavior follows from hyperbolicity of the system and provides the basis for the explicit integration scheme used here. For larger Δt the equations for elements within and including the sonic circle must be assembled and solved simultaneously using an implicit integration approach.

To proceed, it is useful to write the assembled system of model equations as

$$M\ddot{U} = -KU + G \quad (3-31)$$

where U is the global nodal displacement vector, M and K are the assembled mass and stiffness matrices, and G is the global external force vector. The symmetric banded structure of M and K depends on the nodal ordering of U . They are assembled by first switching rows and columns in the element matrices and inflating with rows and columns of zeros so the ordering and spacing of element nodal displacements correspond to the global arrangement

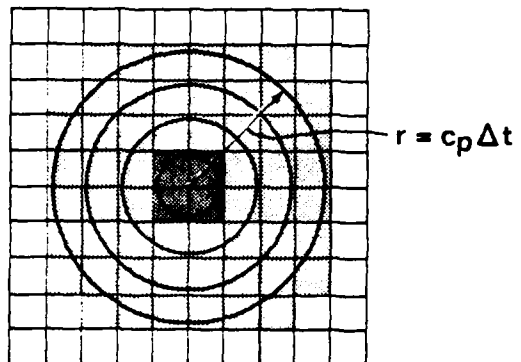


Figure 3-5. A schematic of dynamic interaction between nodes for various Δt measured by the central node's circle of influence (sonic circle).

in \underline{U} ; and second, summing the inflated mass and stiffness matrices to give M and K , respectively.

For explicit integration the internal force vector, $\underline{F} = -K\underline{U}$ need not be assembled but is instead determined by accumulating nodal forces via an element by element evaluation of the element stiffness equation, (3-11). With the right hand side of (3-31) known, the incremental form of the equations is

$$M \frac{\Delta \underline{\dot{U}}}{\Delta t} \approx \underline{F} + \underline{G} \quad , \quad (3-32)$$

whence the equations for velocity increments over the timestep become

$$M \Delta \underline{\dot{U}} \approx \Delta t (\underline{F} + \underline{G}) \quad (3-33)$$

This is recognized as the incremental impulse-momentum equality. The resulting integration algorithm includes the following steps,

1. $\Delta \underline{\dot{U}} = M^{-1} \Delta t (\underline{F} + \underline{G})$
2. $\underline{\dot{U}} = \underline{\dot{U}} + \Delta \underline{\dot{U}}$
3. $\Delta \underline{U} = \Delta t \underline{\dot{U}}$
4. $\Delta \underline{F} = -K \Delta \underline{U}$
5. $\underline{F} = \underline{F} + \Delta \underline{F}$
6. $\underline{G} = \underline{G} + \Delta \underline{G}$

(3-34)

where the external force increments, $\Delta \underline{G}$, are assumed given in the problem definition. Returning to step 1, the process is repeated for the next and subsequent timesteps. In this algorithm nodal velocities should be considered mean values, hence are formally evaluated at the timestep midpoint, while forces and displacements are evaluated at each timestep. However, in applications to linear problems no distinction need be made. Note that nodal displacements are not calculated during the integration, as only increments are used to find $\Delta \underline{F}$ thus \underline{F} .

To solve for $\dot{\Delta U}$ in (3-33) it is necessary to premultiply by the mass matrix inverse, which requires assembly and inversion of the global mass matrix and complicates the algorithm considerably. The explicit scheme averts these global matrix operations by diagonalizing the mass matrix using the lumped mass approximation. On the element level this amounts to replacing M_e defined in (3-14) by $mI/4$ where I is the identity matrix and m is the element mass, $\rho\Delta x\Delta y$. Assembling the global mass matrix yields a diagonal form, with each nodal entry having $1/4$ the mass of contiguous elements.

From the previous analysis of element dynamics the effect of mass lumping is easily found. The relation between modal and nodal element mass matrices is $M_m = S^T M_e S$ so that $(M_m)_{\text{lumped}} = S^T (mI/4) S = mI/4$, whence. $(M_m)_{\text{lumped}} = (M_e)_{\text{lumped}}$. Comparing M_m in (3-25) to $(M_m)_{\text{lumped}}$ shows that the lumped mass is $3/4$ of the consistent mass for extensional and shear modes and $9/4$ for bending modes. Substituting into (3-28) - (3-30) gives $(\omega)_{\text{lumped}}/\omega = 2/\sqrt{3} \approx 1.15$ for extension and shear, and $(\omega)_{\text{lumped}}/\omega = 2/3 \approx 0.667$ for bending.

3.7 Further Development

This final form of the explicit finite element algorithm could have been written more directly than the above derivation indicates, with only minor recourse to theory (or a textbook) for the stiffness matrix. However, the requirements of this study--to solve very large problems as efficiently as possible on supercomputers--warrant a closer look at the basic algorithm. The above exposition and theory are the basis for a more effective formulation of cartesian finite elements.

The theory is developed here to a level commensurate with the algorithm embodied in the FORTRAN code applied in Section 2. However, the theory can be

carried further. In particular, the idea of applying a linear transformation to diagonalize the element mass matrix can be applied to the element stiffness matrix yielding the free vibration modes in Fig. 3-4, which further reduce the operations count. This provides a bonus in that mathematically consistent frequency independent damping can now be selectively defined for each of the element vibration modes, e.g., the pure dilatational and pure shear modes. This is equivalent to Rayleigh damping in the canonical stiffness basis and appears to be a new implementation of damping in explicit finite element codes (for which frequency independent damping has always been a problem). Furthermore, the global assembly of element equations in cartesian coordinates is facilitated by linear transformation to diagonal mass and stiffness matrices because the inflated transformation matrices have very simple inverses.

These concepts will be explored fully in the second part of this research study involving the effects of material damping and three-dimensional modeling. Results will be reported in a second and final report.

SECTION 4

SUMMARY AND CONCLUSIONS

This study was motivated by the need to understand free-field ground motions over laterally inhomogeneous models of the Earth's crust--specifically, graben basins typical of the Basin and Range province. To address this question on the physical scale of a nominal graben basin, i.e., 16 km long, 2 km deep with wavelengths as small as 500 meters, requires a level of wave propagation computing power approximately one order of magnitude greater than scalar computers allow (e.g., CDC 7600). This scale of computation necessitates using a powerful vector computer on the order of a CRAY-1 or CYBER 205 to be economically feasible. However, in addition to a supercomputer, an efficient vectorized algorithm is necessary to approach the theoretical limit of performance. This report has addressed both the seismological calculations in three basin configurations, executed on the CRAY-1, and the finite element theory used to formulate them.

4.1 Summary of Calculations

Synthetic seismograms over the basin flank models are characterized by the relative strength or weakness of a few principal phases. Typical travel time curves for these phases, obtained from the synthetic seismograms, are drawn in Fig. 4-1. Inside the basin, the first coherent arrivals are P-waves, designated Ph 1 in the figure, including direct refracted as well as reflected and diffracted waves from the interface. The second arrivals, Ph 2, are S-waves following similar travel paths within the basin. These S-waves may have sufficient amplitude to reflect significant Rayleigh waves, Ph 3, by mode conversion at the basin edge. The direct Rayleigh wave, Ph 4, is the strongest phase in all cases and reflects a weaker Rayleigh wave, Ph 5, back into the basin.

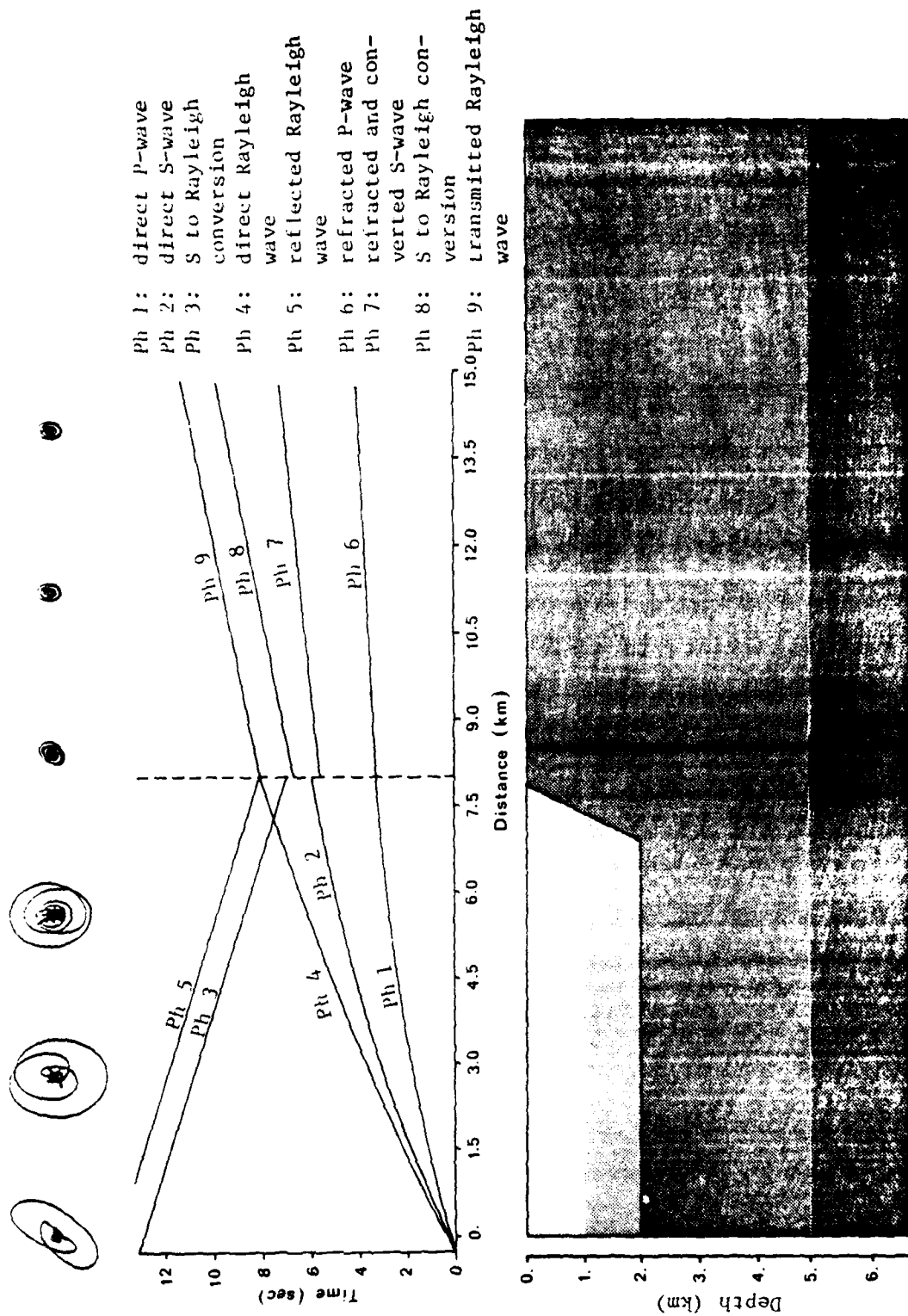


Figure 4-1. A schematic of travel time curves for the principal phases observed in basin flank synthetic seismograms.

Outside the basin, the principal body wave phases include a refracted P-wave, Ph 6, and a refracted S-wave, Ph 7, probably including a transmitted S-wave from the interior. The next arrival is a mode converted Rayleigh wave, Ph 8, from the S-wave within the basin. This phase is typically offset in time, probably due to a strong phase shift in the conversion process near the edge. The strongest phase outside the basin is the transmitted Rayleigh wave, Ph 9, from the direct wave in the basin.

The phases shown in Fig. 4-1 are incomplete in that there are a number of other very weak arrivals discernable in the seismograms, but difficult to identify visually as to source and type. Also, the actual ray paths and mode conversion mechanisms, i.e., multiple reflections, diffractions, etc., of the identified phases require more careful study to quantify. Therefore, the above descriptions should be considered very qualitative, subject to a careful ray analysis to identify single and multiple paths, and higher frequency finite element analysis to allow better separation of phases in time for amplitude estimates.

The basin-range-basin model and calculations extend the physical scale of modeling to include the interaction of two basins separated by a mountain. This demonstrates the practicality of very large-scale calculations, i.e., greater than 100,000 elements, on the CRAY-1. The resulting synthetic seismograms show phases very similar to those described above for the basin flanks and do not indicate any strong modification by the mountain. However, in the second basin the phases are quite complex, caused by incident body and surface waves interacting with the basin's leading edge. This is in contrast to the simple surface source applied to the left basin centerline and requires additional analysis to quantify the resulting phases. The strongest phase is

certainly the direct Rayleigh wave which does not appear to be strongly affected by the mountain and couples efficiently into the second basin. Mode converted S-waves (Rayleigh to S-wave) from the leading edge are the strongest body wave phases within the second basin.

The effects of basin interface geometry, source type, and velocity functions can be briefly summarized. The principal observation is that basin edges are efficient transmitters of Rayleigh waves, apparently independent of the edge details. Rayleigh wave reflection depends strongly on the edge slope, with steep edges better reflectors than dipping edges. Body waves inside a basin are affected by interface shape to some extent, although less than might be expected. Higher frequency analysis is needed to clarify details. Shear waves outside a basin depend markedly on the edge geometry due to mode conversion of waves in the interior. These conversions favor S-waves for the steep flank and Rayleigh waves for the dipping flank. The above observations apply to the normal surface source. The tangential surface source generally excites higher amplitude shear waves within the basin favoring stronger mode conversions (S to S and S to Rayleigh) at the basin edge. Comparing the two loading cases, the obvious feature outside the basins is the strong S-wave for the tangential source in the echelon faulted and dipping flank, with little or no converted Rayleigh wave. This situation is reversed for the steep flanked basin. In terms of velocity functions, synthetics for the constant velocity cases are qualitatively similar to the velocity gradient cases but lose much of the detail. They are, therefore, instructive but not quantitatively useful in modeling real structures.

4.2 Summary of Finite Element Theory

Solving for seismic waves in completely inhomogeneous elastic media requires some form of numerical analysis, based either on ray or wave theory.

However, only wave theory provides complete solutions (in the sense that all wave types are included). The most common implementations of wave theory use finite difference or finite element discretizations. For reasons of efficiency and accuracy (because they provide a closer link to the fundamental mechanics of the seismic medium), finite element methods are preferred here. Time integration of the finite element equations is performed using an explicit approach, which is very efficient for transient phenomena, in contrast to implicit methods. The two-dimensional computational mesh is a simple cartesian grid with a stepwise resolution of material interfaces.

The finite element algorithm is implemented in FLEX, a standard FORTRAN computer code designed for highly efficient processing on scalar, as well as vector computers. A brief summary of the algorithm follows. A finite element displacement approximation over rectangular elements yields elastic force resultants at the nodes, while a lumped mass approximation provides the inertial force resultants. The nodal distribution of lumped masses is moved incrementally in time according to the discrete impulse-momentum equality, with the incremental elastic restoring forces at each node accumulated from contiguous elements. The global time increment is chosen smaller than the shortest transit time across any element, yielding a stable explicit integration algorithm for the uncoupled system of discrete equations. A normal impedance type boundary condition is included to mimic a transmitting boundary (approximately).

The theory described in Section 3 is aimed at reducing the number of arithmetic operations required to evaluate the finite element equations. The standard engineering implementation of finite elements allows general skewed elements, but when rectangular elements only are used, much simpler closed form expressions result. In particular, it is found that linear transformations exist which

diagonalize the element mass and stiffness matrices, thereby reducing substantially the operations count. These transformations are equivalent to well-known deformational modes in elasticity theory. An added benefit of the diagonalizing transformation on the stiffness matrix is that frequency independent damping may be applied to the pure dilatational and pure shear deformational modes. This is accomplished in a mathematically consistent fashion and adds little computational overhead.

4.3 Conclusions

The conclusions to be drawn from this one-year research effort concern: large-scale seismic modeling on supercomputers; graben basin response in the Basin and Range province; and explicit finite element algorithms. The principal conclusion is that complete, linear elastic, high frequency wave fields in inhomogeneous 2-D media can be economically calculated on a large physical scale using the CRAY-1 supercomputer and a vectorized elastic wave solver. For example, comparisons made elsewhere between this approach and more conventional wave solvers on the CDC 7600 show a speed increase of 100 or more and a size increase of at least 10. Such a jump in computational power allows the analyst to solve problems which could not be contemplated before, and at relatively low cost.

The focus of the computational effort was seismic response of three basins for normal and tangential surface sources. The suite of calculations showed a number of differences between a steep faulted flank, an echelon faulted flank and a dipping flank. They also showed that full field synthetics can be nearly as complicated as real data to interpret, requiring interpretational tools like ray tracing to identify phases. Synthetics were generated by convolving a 2 Hz wavelet with a Green's function from the finite element run, but no comparisons

with other time histories were made. Only a single, multilinear velocity function was used in the modeling (besides the piecewise constant function which was too idealized) and it would be useful to examine variations on the velocity function for a single basin model. No attempt was made to include material attenuation, but the finite element implementation of damping was developed and will be implemented in the second phase of this effort. The normal impedance boundary absorber with element grading near the boundary appeared to suppress boundary reflection for the cases considered. However, a better theory would help to reduce problem size, especially in 3-D applications to be examined in the second phase.

The major result of the finite element theoretical work was that, in the context of cartesian finite element grids, the governing equations can be greatly simplified, and formulated so as to admit selective seismic damping on pure shear and dilatational modes of deformation. In addition, the application of linear transformations on the global, as well as local, level offer the possibility of further reducing operation counts and increasing execution speed of the finite element algorithm. This will be examined in the second phase for 3-D applications.

REFERENCES

- Battis, J. (1981). Seismic Velocity Models for Western Alluvial Basins, Environmental Research Papers, No. 740, Terrestrial Sciences Division, Air Force Geophysics Laboratory.
- Frazier, G. A., J. H. Alexander and C. M. Peterson (1973). 3-D Seismic Code for Illiac IV, Contract No. DNA001-72-C-0154, Systems, Science and Software.
- Healy, J. H. and F. Press (1964). Geophysical Studies of Basin Structures Along the Eastern Front of the Sierra Nevada, California, Geophysics, 29, 337-359.
- Newman and Sproull (1979). Principles of Interactive Computer Graphics, Second Edition, McGraw-Hill Book Co.
- Prodehl (1979). Crustal Structure of the Western United States, U.S. Geological Survey Professional Paper 1034.
- Przemieniecki, J. S. (1968). Theory of Matrix Structure Analysis, McGraw-Hill Book Co.
- Stewart, J. H. (1971). Basin and Range Structure: A System of Horsts and Grabens Produced by Deep-Seated Extension, Geol. Soc. Am. Bull., 82, 1019-1044.
- Thompson, F. A., L. J. Meister, A. T. Herring, T. E. Smith, D. B. Burke, R. L. Kovach, R. O. Burford, I. A. Salehi and M. D. Wood (1967). Geophysical Study of Basin-Range Structure: Dixie Valley Region, Nevada, Final Scientific Report AFCRL-66-848, Air Force Cambridge Research Laboratory, Hanscom AFB, Massachusetts.
- Wojcik, G. L. et al. (1981). Research Into Surface Wave Phenomena in Sedimentary Basins, Final Report AFOSR Contract F49620-80-C-0009, Weidlinger Associates.

